Muon Reconstruction and the Search for Leptoquarks at LHC

Diplomarbeit

vorgelegt der
Fakultät für Physik
der
Ludwig-Maximilians-Universität München

von

Benjamin Ruckert

München, den 27. Juli 2006

Muon Reconstruction and the Search for Leptoquarks at LHC

Diplomarbeit

vorgelegt der
Fakultät für Physik
der
Ludwig-Maximilians-Universität München

von

Benjamin Ruckert

München, den 27. Juli 2006

to my parents

Geheimnisvoll am lichten Tag
Lässt sich Natur des Schleiers nicht berauben,
Und was sie deinem Geist nicht offenbaren mag,
Das zwingst du ihr nicht ab mit Hebeln und mit Schrauben.
Faust
Johann Wolfgang von Goethe

Abstract

This diploma thesis focuses on the reconstruction of high-energetic muons. This simulation study was performed within the ATLAS experiment at the Large Hadron Collider (LHC) which is a pp-collider with a centre-of-mass energy $\sqrt{s} = 14$ TeV. The purpose of this study was to identify muons with strongly overestimated transverse momentum using Monte Carlo simulated data which has been generated using Pythia and run through a full detector simulation. These muons can lead to a faked leptoquark signal, as leptoquark-decays can include high-energetic muons. If leptoquarks exist, only a small number of such events is expected which makes the safe momentum measurement a crucial point. To achieve an optimal reconstruction, selection criteria have been developed which compare the track's χ^2, the particle's η-direction and the reconstructed p_Ts from the different reconstruction algorithms, namely the inner detector standalone reconstruction, the muon spectrometer standalone reconstruction and a combination of both. The selection criteria are used to decide which reconstruction is chosen for a given muon. By using this selection method – contrarily to applying a cut – no events are thrown away. As a result the selection reduces the number of misreconstructed muon p_Ts which leads to a lower background and hence to a higher probability of identifying real leptoquark events.

Zusammenfassung

Diese Diplomarbeit befasst sich mit der Rekonstruktion hochenergetischer Myonen.
Diese Simulationsstudie wurde im Rahmen des ATLAS-Experiments am Large Hadron
Collider (LHC) durchgeführt, bei dem pp-Kollisionen bei einer Schwerpunktsenergie
$\sqrt{s} = 14$ TeV stattfinden werden. Ziel dieser Studie war die Identifizierung von My-
onen, deren transversaler Impuls bei der Rekonstruktion stark überschätzt wurde.
Als Daten dienten mit Pythia generierte Monte Carlo Ereignisse, die eine volle De-
tektorsimulation durchlaufen haben. Die Myonen können zu einem vorgetäuschten
Leptoquark-Signal führen, da Leptoquark-Zerfälle hochenergetische Myonen enthal-
ten können. Falls Leptoquarks existieren, wird nur eine geringe Zahl solcher Ereignisse
erwartet, was die sichere und genaue Identifizierung des Impulses zu einem wichtigen
Ziel macht. Um eine optimale Rekonstruktion zu erzielen, wurden Selektionskrite-
rien entwickelt, die das χ^2 der Spur, den η-Richtung der Flugrichtung des Teilchens
sowie die rekonstruierten transversalen Impulse der unterschiedlichen Rekonstruk-
tionsmethoden vergleichen. Hierbei handelt es sich um die Rekonstruktion des Zen-
traldetektors, des Myon-Spektrometers und einer Kombination dieser beiden. Diese
Selektionskriterien werden verwendet, um zu entscheiden, welche Rekonstruktion
für das jeweilige Myon verwendet wird. Durch die Selektion werden – im Gegensatz
zu einem Schnitt – keine Ereignisse verworfen. Das Ergebnis ist eine Reduzierung
der Anzahl fehlerhaft rekonstruierter Transversalimpulse der Myonen, was zu einem
geringeren Untergrund und damit zu einer höheren Wahrscheinlichkeit führt, einen
Leptoquark-Zerfall zu erkennen.

Contents

I

1 Introduction

Elementary particle physics studies the fundamental particles of nature, the forces on a microscopic scale and the interaction of the particles. As the field evolved technical developments lead to better research methods and hence allows a deeper insight into the microscopic structure of nature. It soon became clear that there is a huge diversity of subatomic particles and the scientists started classifying the *particle zoo*. The Standard Model has been very successful in describing the observed phenomena in particle physics. Still, even after many years of research and attempts to complete the puzzle of the Standard Model, it is not final. There are many open questions and each solution seems to produce another problem. This thesis deals with one of them, namely the identity of leptons and quarks. From the theoretical point of view, an interaction between these particles is quite natural, but a particle decaying into both, a lepton and a quark, has not been observed so far. A possible signal in the ATLAS detector might be a decay into a muon and a particle jet. The muons would have a high transverse momentum and one must be sure that it has been measured correctly. A wrongly reconstructed momentum of a lower momentum muon could fake a leptoquark signal. This thesis deals with the reconstruction and identification of high momentum muons.

In chapter 2 a short introduction to the theoretical background of this thesis is given. Starting with the Standard Model which today is the basis for exploring elementary particles, their properties and interactions. The chapter motivates the interest in physics beyond the Standard Model and introduces an effective leptoquark model, explaining the possible occurrence of these hypothetical particles. The chapter concludes with a short overview of the current experimental results and exclusion limits are given. Chapter 3 is dedicated to computing and the software within the ATLAS experiment. After a short introduction to Athena, the analysis framework, an overview of Grid-computing is presented. Grid-computing will be a crucial part of the networking and computing infrastructure in order to cope with the enormous data rate. As this diploma thesis is based on simulated data, a section about the purpose and the production of Monte Carlo samples is of importance and can be found in the last section of the third chapter. In chapter 4 the experimental setup, the *hardware*, of the ATLAS experiment is explained. The ATLAS experiment will

take place at CERN and hence not only the detector but also the LHC accelerator is described. The description of the subdetectors is followed by a section on the muon reconstruction and the reconstruction algorithms MuID and STACO. In chapter 5 the results of the simulation study and analysis are presented. The aim of this study is the muon reconstruction in the tail of the p_T-reconstruction which means the identification of the misreconstructed muons. As muons with overestimated p_T might produce a fake signal for the leptoquark search, it is critical that we have a trustworthy reconstruction and subsequent identification of these particles. Starting from the track quality, several selection criteria are investigated and finally combined to gather optimal results. Due to low statistics a weighting method has been applied as explained in chapter 5.3. Finally, a comparison of the selection is performed between the mentioned reconstruction algorithms. Appendix A explains the χ^2-method, which has been extensively used for track quality investigation. Appendix B lists the samples used for this study.

2 Theoretical Background

The idea of the atomic structure of matter dates back to ancient greek philosophers like Epicurus or Democritus, but John Dalton was the first to state formally the existence of atoms at the beginning of the 19th century. Ninety years later J.J. Thomson discovered the electron as the first subatomic particle and proposed his plum pudding model. It assumes an atom consists of a soup of positive charges (protons) which includes the electrons – just like the plums in a pudding. Some years later one of his students, Ernest Rutherford, disproved this model as his scattering experiment showed that the protons are concentrated in a compact nucleus. Beginning with the 1950s the research of subatomic particles became tremendously successful and revolutionised our understanding of nature. Rapid development of accelerator and detector technology lead to constantly higher scattering energies and hence the possibility of probing smaller scales. A lot of particles have been found and their classification lead to today's Standard Model (SM) of particle physics.

2.1 The Standard Model

The Standard Model of particle physics describes the elementary particles and the fundamental forces between them. It is a gauge theory which is based on the symmetry group $\mathrm{SU}(3)_C \otimes \mathrm{SU}(2)_L \otimes \mathrm{U}(1)_Y$ (this introduction follows [1]).

We know four elementary interactions, but neglect one – the gravitational force – here, because it is too weak between elementary particles compared to the other forces (table 2.1). The interactions are mediated through vector bosons (Spin 1). The strong force couples to colour-charge and is mediated by gluons. The gluons are massless but carry colour charge – hence they interact among themselves. The strength of the interaction together with the self-interaction yields the very short range of 1 fm. The bosons of the weak force carry weak charges, hence they also couple to themselves. Because of their large mass the range is limited to 10^{-3} fm. The third interaction is the electromagnetic one and the associated bosons are the massless photons.

Interaction	couples to	Boson	Mass (GeV/c^2)	J^P
strong	colour	8 gluons	0	1^-
electromagn.	electric charge	photon	0	1^-
weak	weak charge	$W^\pm, Z^0$	$\approx 10^2$	1

Table 2.1: Bosons and their interactions in the Standard Model

The other group of elementary particles are the fermions (Spin 1/2), namely the quarks and leptons. These particles are arranged in three generations by ascending mass, see table 2.2. Quarks participate in all interactions, leptons do not interact strongly as they do not carry colour-charge. Fermions group into left-handed doublets and right-handed singlets under weak isospin transformations. Each of the 12 particles has an anti-particle which has exactly the same properties, but the additive quantum numbers are opposite, e.g. the charge. In the 1960's Glashow, Salam and Weinberg achieved to unify the electromagnetic and the weak interaction, the so-called electroweak unification: $SU(2) \otimes U(1)$. Despite the fact that so far no experimental results disproved the Standard Model, it is also clear that it is not the final theory to describe nature. For example, the Standard Model makes no predictions about dark matter or dark energy, but both states of energy make up 94% of the whole cosmos. There are many questions yet unsolved [2]:

- How do the fermions and bosons get their masses?

- Is the Baryon- and Lepton number conserved strictly?

- Why do baryons and leptons have the same number of generations?

- Why do baryons and leptons carry the same charge?

- What is the nature of dark matter?

In the next section some models to answer questions beyond the Standard Model are briefly introduced. The focus is set to models which require or imply lepton-quark transitions like those mediated by leptoquarks.

2.2   Beyond the Standard Model

The symmetry between quarks and leptons revealed in the Standard Model motivates the assumption that there might be a fundamental relationship between these particles. The search for new particles beyond the Standard Model involves many

Fermions	Generation 1 2 3	el. charge	Colour	weak Isospin left right	Spin
Leptons	ν_e ν_μ ν_τ	0	–	1/2 –	1/2
	$e^\pm$ $\mu^\pm$ $\tau^\pm$	± 1		1/2 0	1/2
Quarks	u c t	+2/3	r,b,g	1/2 0	1/2
	d s b	-1/3		1/2 0	1/2

Table 2.2: The three fermion generations

different theories [3]. One interesting category are the leptoquarks as many theories predict the existence of these particles. Examples are Grand Unified Theories of both, the "Georgi-Glashow-type" [4] as well as of the "Pati-Salam-type" [5], composite models [6], technicolor schemes [7, 8, 9] and superstring-inspired E_6 models [10, 11].

2.3   The mBRW-Model

Instead of a specific leptoquark model a general ansatz is presented. It is the model proposed by Buchmüller, Rückl and Wyler [12]. It uses a most general effective Lagrangian for leptoquark (LQ) interactions with Standard Model fermion pairs under certain assumptions. Leptoquarks

- have renormalisable interactions

- have interactions invariant under Standard Model $SU(3)\otimes SU(2)\otimes U(1)$ gauge groups

- couple only to SM fermions and gauge bosons

- conserve leptonic number L_l and baryonic number B_q separately.
  The fermionic number $F = 3B_q + L_l$ hence $|F| = 0$ or 2.

The last requirement preserves the protons from decaying. These assumptions lead to the following Lagrangian:

$$\mathscr{L} = \mathscr{L}_{|F|=2} + \mathscr{L}_{|F|=0} \tag{2.1}$$

	$\|F\| = 2$ Leptoquarks				$\|F\| = 0$ Leptoquarks		
LQ	Q_{em}	T_3	Decay	LQ	Q_{em}	T_3	Decay
$S_{0,L}$	$-1/3$	0	$l_L^- u_L$ or $\nu_L d_L$	$V_{0,L}$	$-2/3$	0	$l_L^- \bar{d}_R$ or $\nu_L \bar{u}_R$
$S_{0,R}$			$l_R^- u_R$	$V_{0,R}$			$l_R^- \bar{d}_L$
$\hat{S}_{0,R}$	$-4/3$	0	$l_R^- d_R$	$\hat{V}_{0,R}$	$-5/3$	0	$l_R^- \bar{u}_L$
$S_{1,L}$	$-4/3$	-1	$l_L^- d_L$	$V_{1,L}$	$-5/3$	-1	$l_L^- \bar{u}_R$
	$-1/3$	0	$l_L^- u_L$ or $\nu_L d_L$		$-2/3$	0	$l_L^- \bar{d}_R$ or $\nu_L \bar{u}_R$
	$+2/3$	$+1$	$\nu_L u_L$		$+1/3$	$+1$	$\nu_L \bar{d}_R$
$V_{1/2,L}$	$-4/3$	$-1/2$	$l_L^- d_R$	$S_{1/2,L}$	$-5/3$	$-1/2$	$l_L^- \bar{u}_L$
$V_{1/2,LR}$	$-4/3$		$l_R^- d_L$	$S_{1/2,R}$	$-5/3$		$l_R^- \bar{u}_R$
	$-1/3$	$+1/2$	$l_R^- u_L$		$-2/3$	$+1/2$	$l_R^- \bar{d}_R$
$\hat{V}_{1/2,L}$	$-1/3$	$-1/2$	$l_L^- u_R$	$\hat{S}_{1/2,L}$	$-2/3$	$-1/2$	$l_L^- \bar{d}_L$
	$+2/3$	$+1/2$	$\nu_L u_R$		$+1/3$	$+1/2$	$\nu_L \bar{d}_L$

Table 2.3: Leptoquarks derived from the mBRW model

where

$$
\begin{aligned}
\mathscr{L}_{|F|=2} ={}& (g_{1L}\bar{q}_L^c i\tau_2 l_L + g_{1R}\bar{u}_L^c i e_R^-)S_0 + \hat{g}_{1R}\bar{d}_R^c e_R^- \hat{S}_0 + g_{3L}\bar{q}_L^c i\tau_2 \tau l_L S_1 \\
&+ (g_{2L}\bar{d}_R^c \gamma^\mu l_L + g_{2R}\bar{q}_L^c \gamma^\mu e_R^-)V_{1/2\mu} + \hat{g}_{2L}\bar{u}_R^c \gamma^\mu l_L \hat{V}_{1/2\mu} + h.c. \\
\mathscr{L}_{|F|=0} ={}& (h_{1L}\bar{q}_L \gamma^\mu l_L + h_{1R}\bar{d}_R \gamma^\mu e_R^-)V_{1/2\mu} + \hat{h}_{1R}\bar{u}_R \gamma^\mu e_R^- \hat{V}_{0\mu} + h_{3L}\bar{q}_L \tau \gamma^\mu l_L V_{1\mu} \\
&+ (h_{2L}\bar{u}_R l_L + h_{2R}\bar{q}_L i\tau_2 e_R^-)S_{1/2} + \hat{h}_{2L}\bar{d}_R l_L \hat{S}_{1/2} + h.c.
\end{aligned}
\tag{2.2}
$$

Here q_L and l_L denote the $SU(2)_L$ left-handed quark and lepton doublets and e_R, d_R as well as u_R are the corresponding right-handed singlets for leptons, down-type and up-type quarks. S and V stands for scalar and vector leptoquarks. Further $\Psi^c = C\bar{\Psi}^T$ which is the charge conjugate of the fermion fields. This Lagrangian yields 14 different leptoquarks (see table 2.3) – seven scalars and seven vectors – but in most underlying models (e.g. GUTs) there exists only a subset of them. Two more restrictions lead to the so called "minimal Buchmüller-Rückl-Wyler effective model" (mBRW model) to manage with the existing low-energy constraints:

- LQ each couple to a single lepton-quark generation

- LQ have pure chiral couplings to SM fermions

Moreover these restrictions allow to use only one symbol λ for the different Yukawa couplings (denoted $g, \hat{g}, h$ and $\hat{h}$ in the above Lagrangian). The restriction $\lambda^i \lambda^j \approx 0$ if $i \neq j$ avoids flavour-changing neutral currents (FCNC).

2.4   Production of Leptoquarks

Leptoquarks can either be produced singly (figure 2.1) or in pairs (figure 2.2). At hadron colliders like the (currently being constructed) LHC (pp) or the Tevatron ($p\bar{p}$) the pair production of LQ via $q\bar{q}$-annihilation or gg-fusion prevails. These mechanisms allow the production of leptoquarks of all three generations. In addition single production is possible, but it depends on the (model dependent) Yukawa coupling λ contrarily to the pair production which only uses QCD interactions (in fact there is one suppressed production mechanism through Yukawa coupling contributing only little to the cross-section). So the cross-section for scalar leptoquark pair production does not depend on any parameters, for vector leptoquarks this is not true. Two anomalous-coupling parameters κ_g and λ_g contribute which makes the treatment harder. These parameters can be connected through the anomalous magnetic and electric moment of the vector leptoquark in the colour-field [13]. For vector leptoquarks the production cross-section is larger than for scalar leptoquarks but varies depending on the choices for the parameters. One distinguishes three leptoquark generations, because – due to mentioned constraints – leptoquarks couple only to one quark and lepton generation.
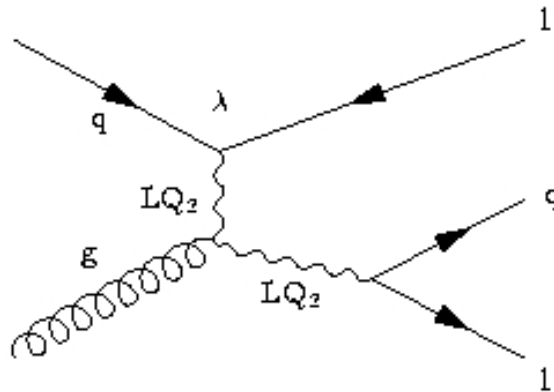

Figure 2.1: Example of leptoquark single production. This process depends on the unknown Yukawa coupling λ

2.5   Experimental Results

Several experiments searched for leptoquarks but none were observed so far. In 1997 the HERA collaboration observed anomalous events which could have been
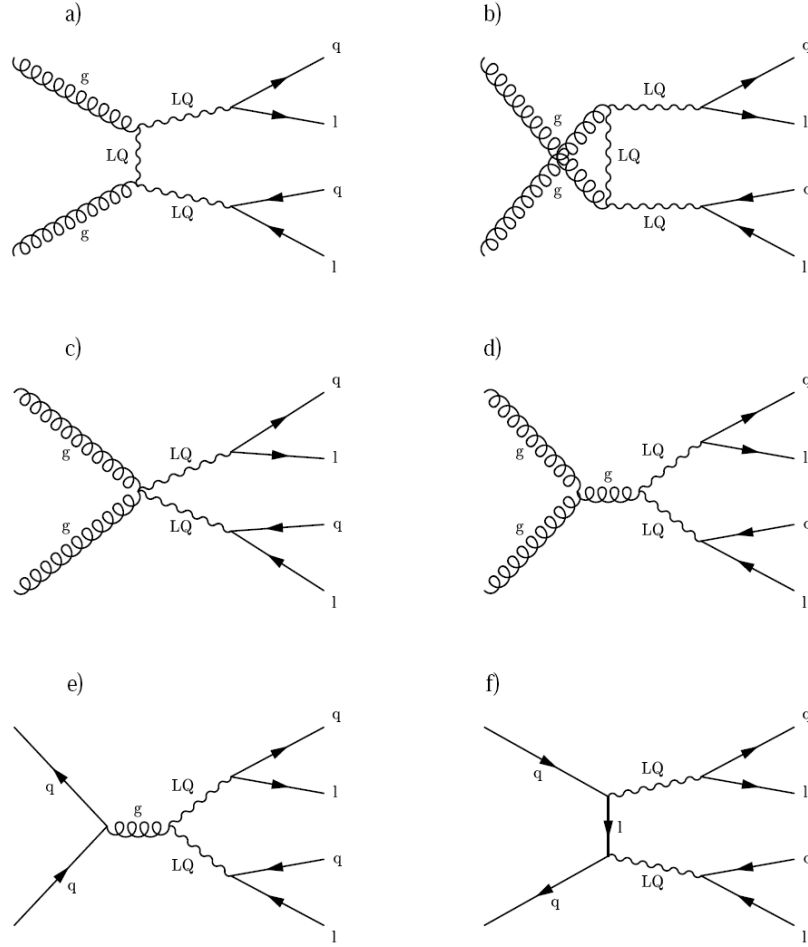
Figure 2.2: Feynman graphs for the LQ pair production.

interpreted as a leptoquark signal but turned out to be a statistical fluctuation [14]. From the HERA as well as the Tevatron experiments bounds on the leptoquark masses have been calculated. For first generation scalar leptoquarks the lower mass limit has been calculated to $M_{LQ} > 242$ GeV[1] at the Tevatron experiment. For vector leptoquarks of the first generation the limit is in the range from 233 to 345 GeV (depending on the model assumptions). For second generation leptoquarks the lower mass limit has been calculated to 222 GeV. The results are valid if the leptoquarks decay in charged leptons and quarks with a probability of 1 [1]. The new LHC accelerator extends the mass reach up to more than 1 TeV (table 2.4), hence increasing the current mass bounds by an order of magnitude. There are three

[1]Throughout the whole thesis the so called Heaviside-Lorentz system of measurement together with natural units is used: $\hbar = c = 1$.

M_{LQ} [TeV]	σ [fb]	Signal	Background	$S/\sqrt{B}$
1.0	4.96	98.5	2.84	58
1.2	1.33	22.0	2.43	14
1.3	0.713	12.8	1.44	11
1.5	0.223	3.62	0.376	5.9

Table 2.4: Signal cross section for first generation, expected number of signal and background events and significance for the $eejj$ channel, for various LQ masses and $L = 30\text{fb}^{-1}$. [3]. For second generation leptoquarks the production cross section is approximately 2% lower and the results are similar. These results have been obtained using fast simulation, this study utilises full detector simulation.

types of final states of the leptoquark pairs: $ll + 2$ jets, $l\nu + 2$ jets and $\nu\nu + 2$ jets where l is a charged lepton and ν stands for the neutrino. The searches for final states containing a neutrino take the missing transverse energy into account. Figure 2.3 shows the exclusion limits for scalar first-generation leptoquarks from various experiments.
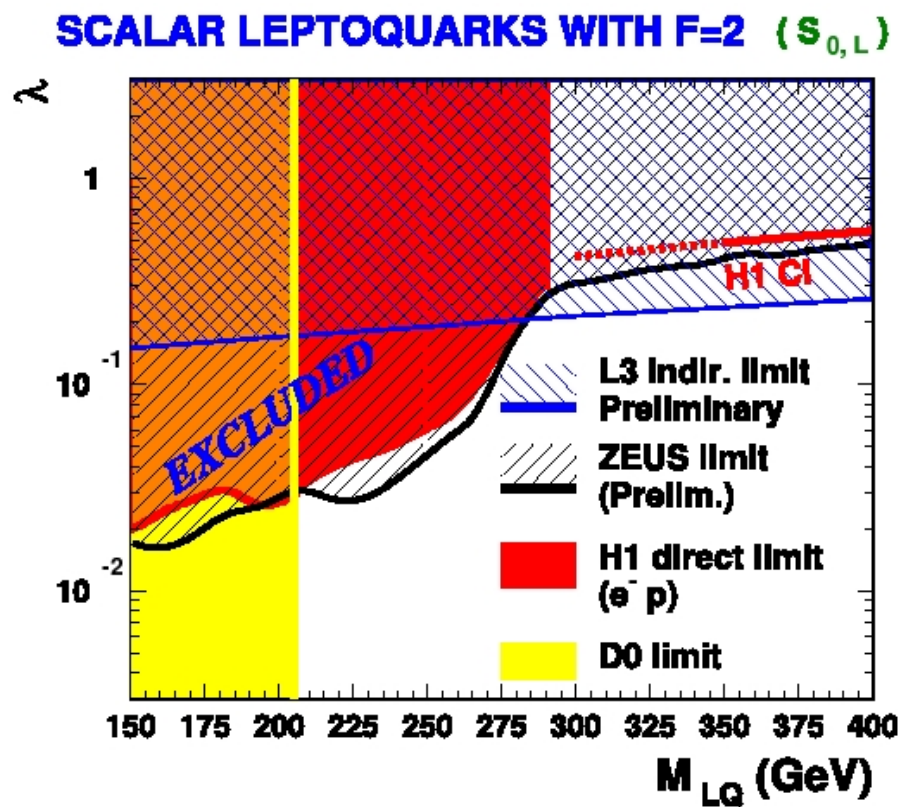
Figure 2.3: Exclusion limits obtained from several collider experiments for scalar first-generation leptoquarks

3 Software and Computing at ATLAS

The LHC and the associated experiments will be very large and challenging. Therefore huge requirements not only for the hardware, but also for the software have to be satisfied. The enormous potential can only be exhausted if the scientists can cope with the huge data rate. Each 25 ns (which equals a rate of 40 MHz) there will be a collision between two bunches resulting in 23 pp collisions. This rate has to be reduced by triggers to 200 Hz which yields a data rate of 3 PB per year. To process and analyse the data new approaches have to be made, one of them is the development of the Grid structure. The Grid is a new kind of computing architecture. It is a virtual model, as it connects many networked computers, e.g. via the internet. It is capable of and designed for distributed computing as it has a parallel infrastructure. Hence it is possible to solve large-scale computing problems, which would be impossible on single computers. Data will be stored in several computing centers (so called Tiers) and the analyses usually will be running on the Grid, not on local computing nodes. The ATLAS framework for computing is called Athena. It provides functionality and communication between different components. Before data taking starts it is essential to understand the detector as good as possible and to stress the computing infrastructure. Both is done using Monte Carlo samples, the latter by generating these samples on the Grid.

3.1 Athena

Gaudi is a software framework for High-Energy Physics. The ATLAS-specific implementation is called Athena. Athena is an interface between user and computing infrastructure and insulates the users from irrelevant details, i.e. which I/O libraries to load. Athena follows some main design principles:

- it uses abstract interfaces to be able to use different implementations providing the same functionality but optimized for certain environments

- it uses dynamic libraries

- it separates clearly between data and algorithms

- it separates clearly between persistent and transient data

The software is configured and controlled via a `jobOptions.py`-file, which is a script written in Python. Advantages of the use of a scripting language are easy configuration, i.e. selection of algorithms and services to be used and its interactivity. The user has the possibility to immediately make changes without recompiling the source code of the analysis.

3.2   Grid-Computing

Grid Computing in this context is referred to as distributed computing for data storage and analyses within the LHC structure. The LHC experiments will produce a huge amount of data, e.g. for the year 2008 a CPU capacity of 140 million SPECint2000 and a capacity of 30 PB disk storage and 50 PB of mass storage are required [17]. Resources and data will be shared among the computing centers, institutes and universities over the whole world. For this purpose a highly reliable and efficient wide area networking structure is necessary. The data of the experiments will be distributed around the world, according to a hierarchical structure (TIERs) and then usually the analysis code is sent to the data (respectively the storage elements), not vice versa. At the startup of LHC and its experiments in 2007 it is necessary for the Grid and the computing infrastructure to be fully operational. To achieve this data challenges and service challenges are executed to probe and evaluate the current infrastructure. Within the LHC structure there are three different Grid flavours (LCG, NorduGrid, OSG) which have to be fully interoperable. To cope with this requirements a specialized software to manage data distribution and access rights (authentication, authorization, job submission) is needed. This software, referred to as "Middleware", provides the communication between the user and the Grid, and has to be flexible, yet simple to allow convenient working for the scientists without having to pay attention to the underlying Grid structure. An example for this kind of software – which is also used within ATLAS – is "gLite". The Tier structure is as follows:

- Event Filter: near experiment

- Tier 0 (CERN):

    - stores the raw data at mass storage

  - produces ESD[1] and AOD[2]
  - ships ESDs, AODs and raw data to Tier 1s

- Tier 1 (10 worldwide):

  - re-reconstruction of raw data every 1-2 months using better calibration
  - produce new AODs and ESDs
  - reprocess all resident raw data once per year with best calibration and software available
  - overall storage $\approx$ 10 Petabyte

- Tier 2 ($\approx$ 30 worldwide):

  - Monte Carlo Simulations
  - on demand: user physics analyses
  - overall storage $\approx$ 20 Petabyte

- Tier 3 (distributed worldwide):

  - physics analyses

3.3 Monte Carlo Production

Monte Carlo Simulation is a statistical method which bases upon the usage of random variables, respectively on performing a random process very often, hence it is named after the famous monegasque quarter Monte Carlo which is well-known for its casinos. The method has been developed in the 1940s for the theoretical research of the interaction of neutrons with matter in the context of building the nuclear bomb within the Manhattan project. The method allows the numerical solution of problems using stochastics. An analytical solution of such problems usually is not possible. The method bases upon the law of large numbers. From a mathematical point of view, it is a trajectory in the phase space which is weighted by its probability. Monte Carlo Integration is useful for calculating average values

$$\langle A \rangle = \sum_{x \in \Omega} P(x) A(x) \tag{3.1}$$

---

[1]Event Summary Data, see 3.3.2
[2]Analysis Object Data, see 3.3.2

or high-dimensional integrals

$$\int_{x\in\Omega} P(x)A(x)d^n x \qquad (3.2)$$

where $P(x)$ denotes the statistical weight, $A(x)$ is the value of A in state x and Ω is the particles phase space in the system. An advantage of Monte Carlo methods is their increasing efficiency with growing dimensions, i.e. their error $\propto 1/\sqrt{N}$, while for numerical integration using Simpson's rule the error $\propto 1/\sqrt{N^{4/n}}$. Furthermore, only few points are needed to get a first estimate ("feasibility limit") and every additional point improves the accuracy ("growth rate"). A disadvantage is the relatively slow convergence in few dimensions.

But the Monte Carlo method is not only a simple numerical integration method from the mathematical point of view, because it can be used also to describe and simulate physics processes. For example, $P(x)$ equals a statistical weight and $A(x)$ is the value of a certain function A in the state x. This could be a fragmentation function or a differential cross section.

One of the event generators used for ATLAS is Pythia [18]. An event generator produces certain particles and simulates their decay according to the specific decay modes. In real data, the branching of an object into a small number of subsequent particles is described by the statistical fluctuations through quantum mechanics. In event generators Monte Carlo techniques are used to select the relevant variables according to probability distributions. Starting from the originating particle to the final state a kind of a tree structure evolves. The particle recursively decays at each branch randomly and yields everywhere a non-ambiguous chain until a stable particle is left. An event generator is usually validated by comparing it with experimental results and other event generators.

GEANT4 is a software packet suitable for simulating the passage of particles through matter. At ATLAS it is used for full scale detector simulation and is integrated within Athena. It includes all aspects of the simulation process like geometry, material, tracking of particles through materials and external electromagnetic fields, detector response and capture for subsequent analysis. It covers the complete energy range up to several TeV.

The ATLAS detector will produce several Petabyte of raw data per year, which makes the distribution to collaborators nearly impossible. Hence strategies to provide institutes with essential data had to be developed. The result are different types of datasets, which are available:

- Raw Data Object (RDO): a C++ object representation of the data flowing from the High Level Trigger

- Event Summary Data (ESD): is built after the reconstruction and contains the complete output of the reconstruction. It is usually not needed for physics analyses, but more intended for the needs of detector calibration and improvement of reconstruction algorithms. The target size is 500 kB per event.

- Analysis Object Data (AOD): it can be produced from the ESD and contains a summary of the reconstructed event. The information included will suffice for most physics analyses. The target size is 100 kB per event.

3.3.1   Data Challenges

Before the startup of ATLAS the computing infrastructure as well as the detector has to be understood and optimized. The computing infrastructure is tested by distributed simulation and production of Monte Carlo Samples. The production and distribution is a huge effort and therefore a good stress test for commissioning. The production of physics samples with adequate statistics is nearly impossible for single persons or institutes as the process needs very high computing power and time. That is why large samples are produced centrally. In 2005 the so called Data Challenge 2 has been accomplished, with the focus on the production of samples. In 2006 the Commissioning Service Challenge (CSC) was started, whose main purpose is the test of the infrastructure.

3.3.2   Full Simulation

There are two methods to produce Monte Carlo samples for simulation. The first one is the so called Full Simulation. This mode consists of several steps described below (see also figure 3.1):

- Generation: in the first step, the events will be generated using an event generator like Pythia. Starting from a given physics process, the properties of the particles are calculated (four-vectors).

- Simulation: the generated events are processed using a GEANT4 Simulation of the detector. Thereby GEANT4 hits are produced, i.e. trajectory of the particle and its deposited energy.

- Digitization: now the GEANT4 hits are processed and thereby the response of the detector is considered, which produces Digits, such as voltages or drift-times. Just like the real data.

- Reconstruction: the raw-data digits then are reconstructed into tracks and energy deposits and stored in an Event Summary Data (ESD).

- Create Analysis Object Data (AOD): The AOD simply contains not all, but still sufficient information for physics analyses.

3.3.3 Fast Simulation

The fast simulation of ATLAS events with the so called Atlfast package produces the AODs directly from the Generation of the events (see figure 3.1). The input contains the four-vectors of the physics event. It does not use the full detector simulation and reconstruction, but smears the Monte Carlo Truth information from the generator, for example the energy deposits. Furthermore the track helix parameters and quantities as E_T and $p\!\!\!/_T$ are calculated by Atlfast. The whole process uses information achieved from full simulation. A big advantage of Atlfast is the low time consumption compared to full simulation – Atlfast is approximately 4-5 orders of magnitude faster.

To study the behaviour of particles traversing the detector and their reconstruction is the aim of this analysis, hence it needs full simulation and not the smeared Monte Carlo Truth information from the generator.
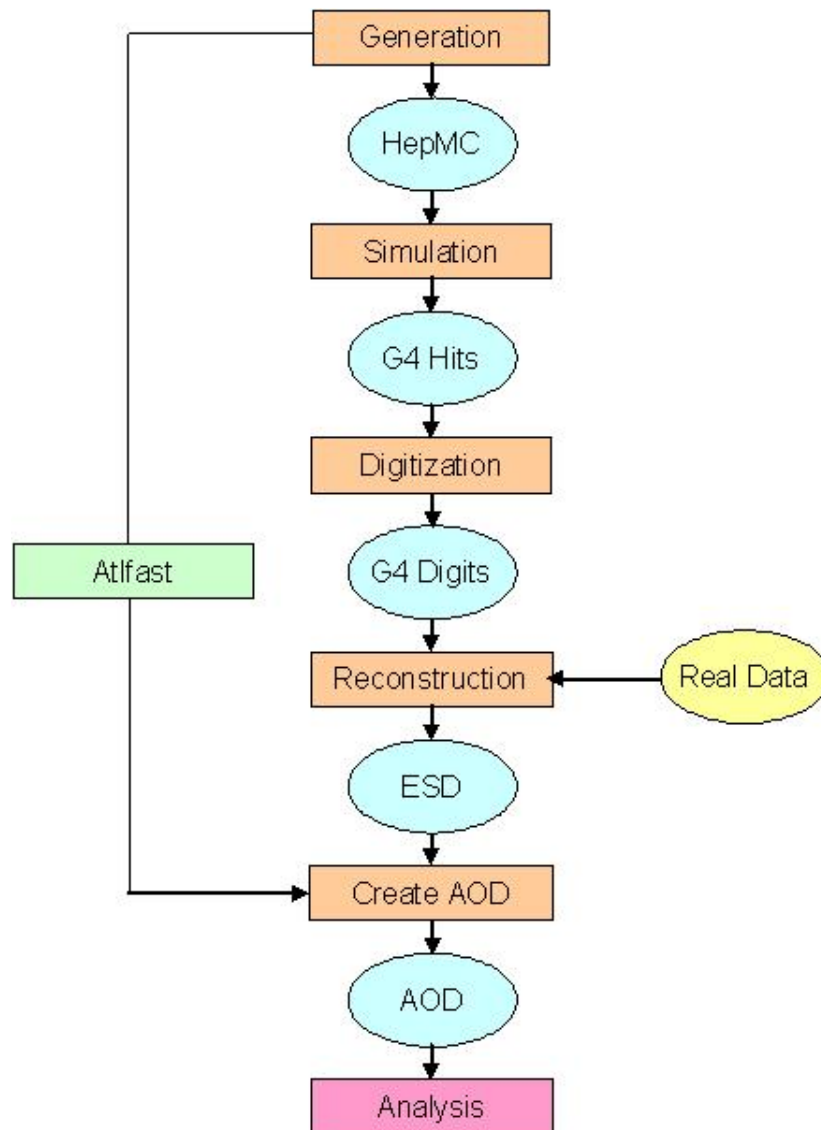
Figure 3.1: Full and Fast Simulation of Samples for ATLAS

4 The LHC and the ATLAS Experiment

The Large Hadron Collider (LHC) at CERN[1] will be the particle accelerator with the highest energy built so far, the planned start-up is 2007. The need for increasingly powerful accelerators and sensitive detectors is justified because the mass of the produced particles depends on the colliding particles centre-of-mass energy $\sqrt{s}$. One of the main goals of the LHC will be the search for the Higgs particle, which is an additional boson that could be responsible for all particles masses via the mechanism of spontaneous symmetry-breaking. The existence of the particle could not be proved so far and hence a mass $M_H < 114.4$ GeV [19] is excluded experimentally. Amongst others the experiments at Tevatron and LEP have searched for this particle. But aside from the Higgs search and precision measurements of Standard Model parameters (e.g. W and top mass and mixing parameters), LHC and its experiments will probe for more exotic particles and underlying theories like SUSY[2], Black Holes or leptoquarks.

4.1 The Large Hadron Collider

The LHC is a *pp*-collider with a centre-of-mass energy of $\sqrt{s} = 7$ TeV per beam, which means that the centre-of-mass energy at which protons collide is 14 TeV. The bunches of protons are accelerated and stored in a ring of 27 km circumference. The particles move nearly at the speed of light, which means they traverse the storage ring more than 10000 times a second. One characteristic quantity of an accelerator is the luminosity which is expected to be 10^{34} cm^{-2}s^{-1} for LHC. On average, each bunch collision will produce 23 *pp*-collisions.The LHC uses the existing accelerator structure from earlier experiments to pre-accelerate the protons to 450 GeV before injecting them into the LHC. The LHC cryostats consist of two separate

---

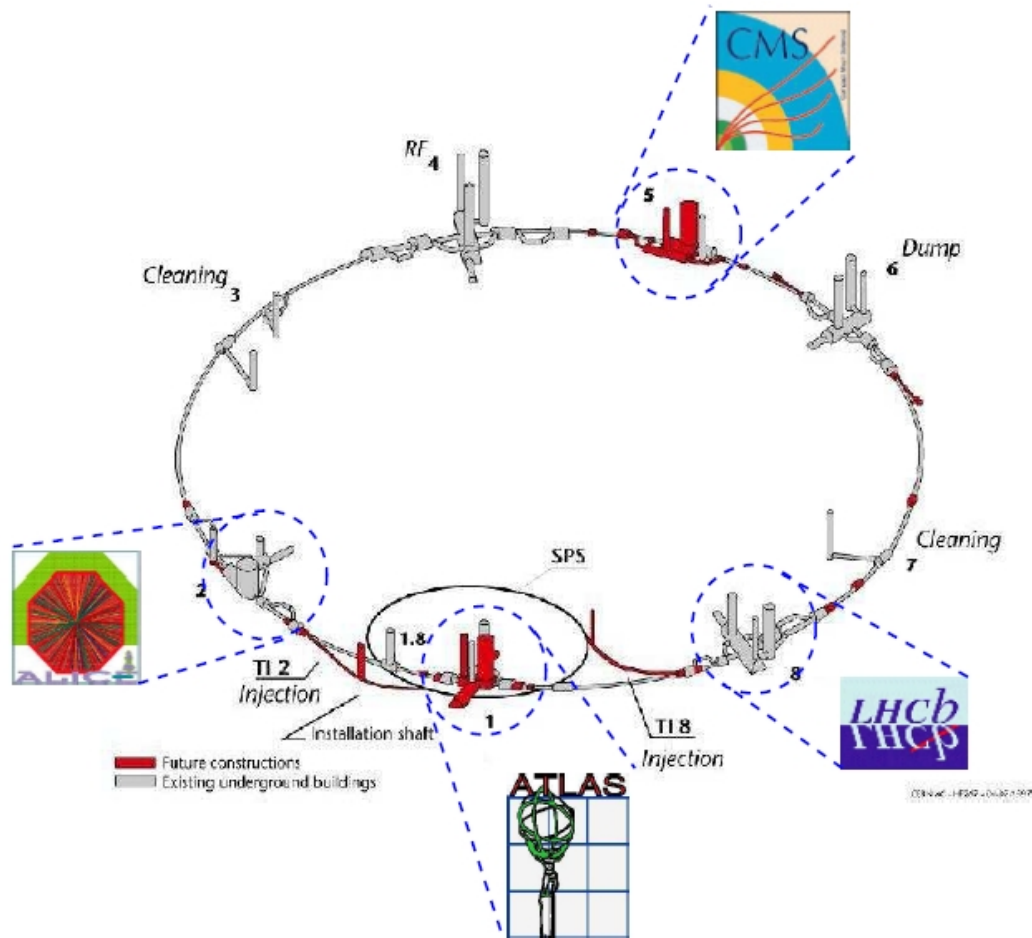[1]Organisation Européenne pour la Recherche Nucléaire
[2]SUperSYmmetry

Figure 4.1: schematic view of the LHC and the associated experiments [20]

tubes and contain magnets in order to bend the same-sign particles circulating in opposite directions. The pipe is surrounded by superconducting dipole magnets which have a strength of 8.4 Tesla. At four points the separated beams will collide and around those points the experiments – ALICE, ATLAS, CMS and LHCb – are being built. In addition to the proton-proton collisions there is also a mode for the acceleration of lead atoms with a maximum colliding energy of 1.1 PeV (this equals 2.76 TeV/nucleon).
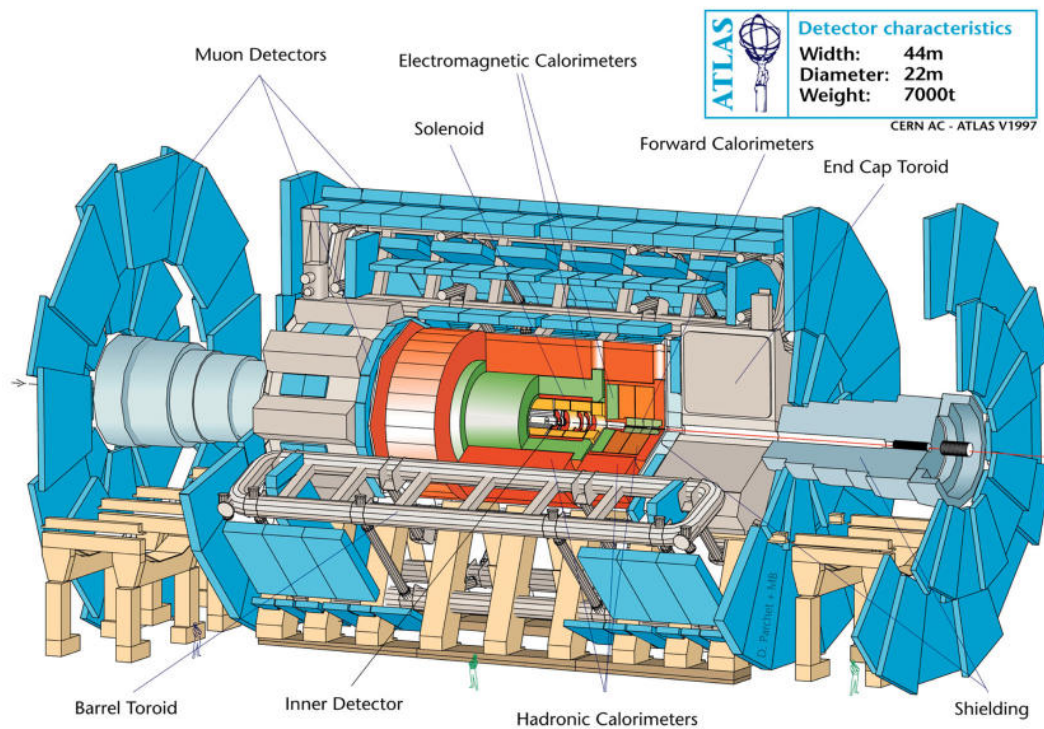
Figure 4.2: 3-dimensional view of the ATLAS detector [20]

4.2 The ATLAS Detector

ATLAS[3] is one of four main experiments at the LHC. Weighing 7000 t and being 22 m in diameter and 44 m long, it is one of the largest and heaviest particle detectors hitherto built for accelerator experiments. The detector uses the same cylindrical geometry as most collider detectors: it has a barrel region and two end-caps (figure 4.2). The components of the detector are arranged in several layers, just like an onion.

4.2.1 The Inner Detector

The Inner Detector contains three subdetectors, namely the pixel detector, the Semiconductor Tracker (SCT) and the Transition Radiation Tracker (TRT). The pixel detector has three so called B-Layers, which are essential for good vertexing. The SCT, which, in combination with the pixel detector, is referred to as "Precision

---

[3]A Toroidal LHC ApparatuS

Tracker" is made of some double layers of silicon strips aligned in the azimuthal direction where the second layer is rotated by a stereo angle with respect to the first. The outer sub-detector (TRT) is made of straw tubes and a radiator (between the tubes) to stimulate transition radiation from electrons. Each of the 420,000 channels provides a drift time measurement and two independent thresholds, which allow the detector to discriminate between tracking hits which pass the lower threshold and transition radiation hits which pass the higher one. A main design goal of the TRT was its good performance at high occupancy and counting rates. The momentum measurement depends on the direction of the magnetic field (the global ATLAS coordinate system is introduced in figure 4.3). The Lorentz-Force

$$\vec{F}_L = q \cdot \vec{v} \otimes \vec{B} \qquad (4.1)$$

is perpendicular to the magnetic field. This means that a particle is curved in a plane perpendicular to the magnetic field. Because the measurement of the momentum depends on the curvature, it also depends on the configuration of the magnetic field. The magnetic field created by the solenoid ($\vec{B} = 2$ T) in the inner detector is parallel to the beam axis, hence charged particles are curved in the x-y-plane, which is also the p_T-plane. Therefore the momentum resolution is proportional to $1/p_T$. On the other hand, the magnetic field created by the toroid (which is not uniform) leads to magnetic field lines in the x-y-plane. Because the particles are curved perpendicular to that plane and the momentum measurement in principle is done through the determination of the deviation from a straight line (see also the paragraph about the sagitta 4.2.3) the resolution is proportional to $1/p$. Using the curvature r the p_T can be calculated from

$$p_T = q \cdot B \cdot r \qquad \text{with} \qquad p_T = p \cdot \sin\theta \qquad (4.2)$$

4.2.2 The Calorimeters

Calorimeters in principle measure the energy from particles by absorbing them. The calorimetry at ATLAS uses two types of calorimeters, the electromagnetic (EM) and the hadronic calorimeter. The EM calorimeter is a lead/liquid argon detector installed in a barrel cryostat, which also contains the solenoid for the Inner Detectors magnetic field. The converter plates of the EM calorimeter have accordion geometry, the ϕ symmetry is disturbed and there are other means to avoid azimuthal cracks. e and γ showers are precisely measured in the electromagnetic calorimeter. The main purpose of the hadronic calorimeter is the measurement of the transverse energy, high-energetic jets, respectively particles which mainly interact hadronically with the atoms of the absorber ($\pi, p, n...$). The Tile calorimeter (in the barrel region) is
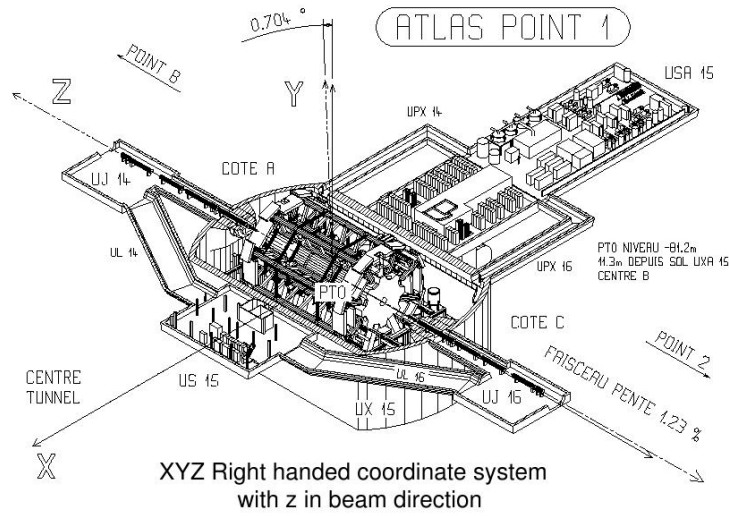
Figure 4.3: This figure shows the ATLAS coordinate system. It is a right-handed coordinate system with the z-axis in beam direction, the y-axis pointing upwards and the x-axis pointing towards the centre of the LHC ring. The polar angle $\theta = 0$ is defined as the positive z-axis and the azimuthal angle $\phi = 0$ is defined as the positive x-axis.

a sampling calorimeter where iron serves as absorber and scintillating tiles as active material. The hadronic end-cap and forward calorimeters use liquid argon due to its intrinsically high radiation resistance.

4.2.3 The Muon Spectrometer

The outermost part of the ATLAS detector is the muon spectrometer (see figure 4.5). Charged particles passing the Inner Detector and the calorimeters will be deflected in the large toroidal magnetic field (the integrated bending power reaches from 3 Tm up to 8 Tm). The coils of the toroid will be cooled down to 4.5 K using liquid helium. The system itself is a combination of several subdetectors, but the most important part are the Monitored Drift Tubes (MDTs), which are responsible for the measurement of the tracks. The muon tracks are measured at three distances from the interaction point in the muon spectrometer to be able to determine the muon momentum from the sagitta [21] (figure 4.4). Let r be a circles radius (i.e. the trajectory of a charged particle in a constant magnetic field) and let d be the length of a straight line between the endpoints of the circle segment. Then the sagitta s is defined by the height of the circle segment. It can easily be calculated from
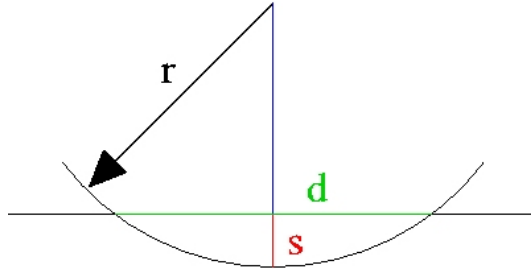
Figure 4.4: This plot illustrates the determination of the sagitta s.

$$(r - s)^2 + \left(\frac{d}{2}\right)^2 = r^2 \tag{4.3}$$

Using equation 4.2 then yields the transverse momentum p_T. In high-η regions and close to the interaction point instead of the MDTs so called Cathode Strip Chambers (CSCs) are used due to their higher radiation resistance. The CSCs are multi wire proportional chambers with cathode strip readout. The coordinates are measured via the charge induced on the segmented cathode by the avalanche on the anode wire. Segmentation of the readout cathode leads to a good spatial resolution. To achieve high accuracy despite the huge dimensions of the spectrometer, an optical alignment system has been developed; it measures the relative positions of the chambers and thus improves the precision of the reconstruction. The trigger system employs Resistance Plate Chambers (RPCs) in the barrel region and of Thin Gap Chambers (TGCs) in the end-cap region. The RPCs are gaseous detectors with no wires in it. The primary ionisation electrons are multiplied into avalanches by a high electric field. The signals are readout via capacitive coupling by metal strips on both sides of the detector. The RPCs have a very good intrinsic time resolution. The TGCs in principle are multi wire proportional chambers, but with the difference that the anode wire pitch is larger than the cathode-anode distance. The anode wires are parallel to the MDT-wires and provide, together with the readout strips, the trigger information. These strips are also used to measure the second coordinate.

4.2.4   Muon Reconstruction and Algorithms

As mentioned above, the muon tracks are measured by the muon system as well as by the inner detector; then the tracks are reconstructed by the hits in these subdetectors. This leads to three different reconstruction methods for the muons:
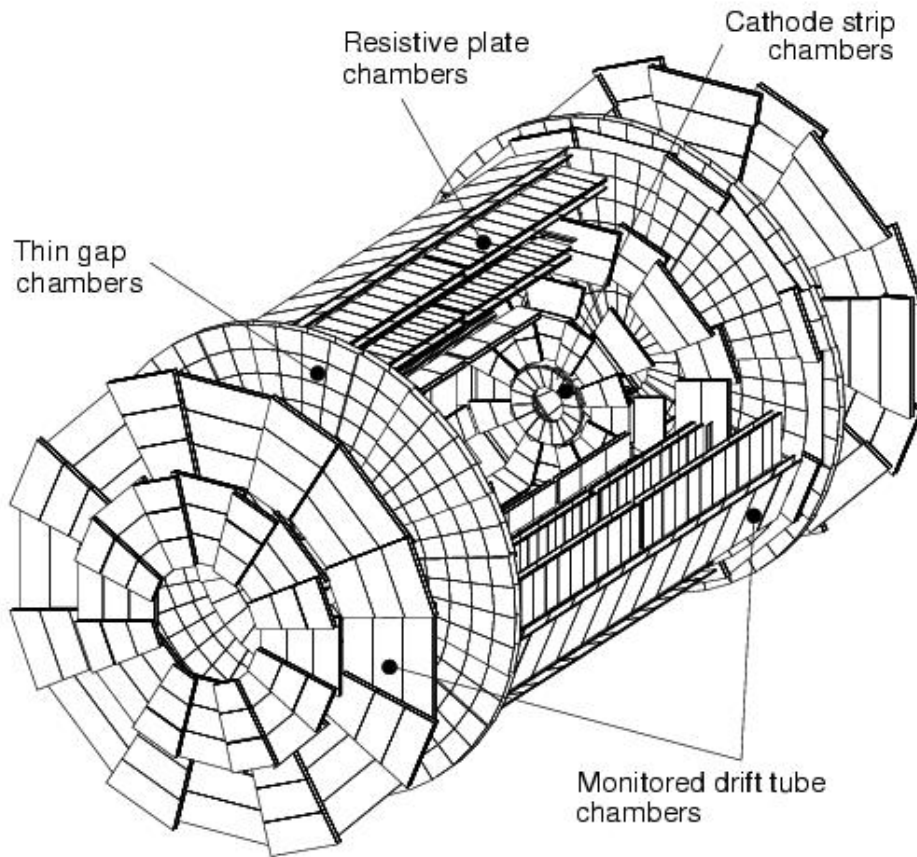
Figure 4.5: The ATLAS Muon Spectrometer [20].

- Inner Detector standalone

- Muon Spectrometer standalone

- using a combination of both

For analyses the user has access to all three of these reconstructed tracks and each method has advantages and disadvantages. As we will see, in general the combination of inner detector and muon spectrometer tracks yields the best results. But this is not always true, which means that for special purposes standalone reconstruction
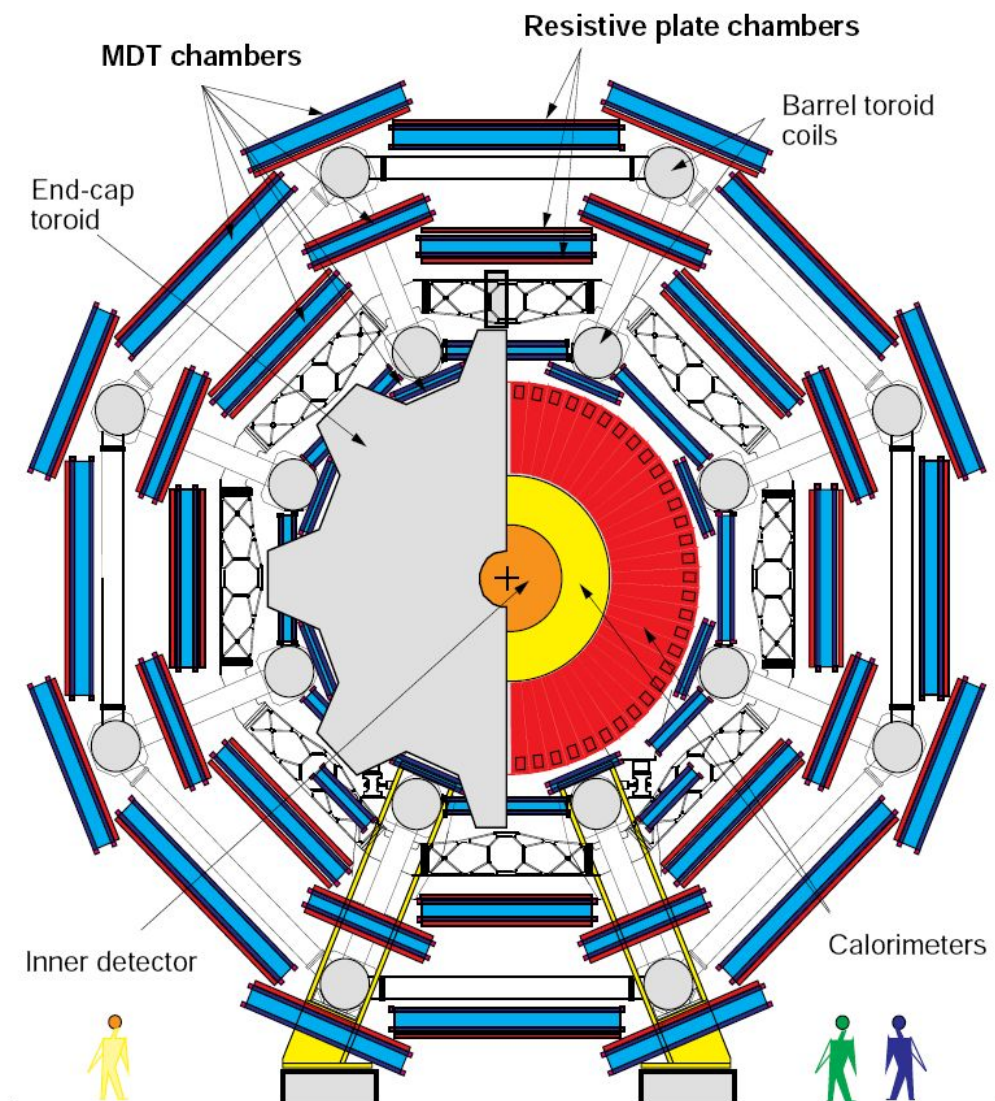
Figure 4.6: Transverse view of the ATLAS detector [20].

can lead to better results. In ATLAS muons are currently reconstructed with two independent packages, one is based on the statistical combination of two independent measurements (ID and muon spectrometer) using the covariance matrices of the reconstructed tracks. This procedure is called STACO[4]. The second strategy, which is called MuID, fits the global muon track by using the hits from two subdetectors. Now the several reconstruction algorithms for the inner detector track and the muon spectrometer track as well as the algorithms for combining both are introduced.

iPatRec

iPatRec[5] utilises several packages for track finding, fitting and extrapolation through an inhomogeneous magnetic field and is used for the inner detector. The subalgorithms use a geometry database, which is created at the initialisation and describes the precision tracker as well as a parameterized version of the magnetic field. For the reconstruction at first adjacent raw-data channels are clustered and spacepoints are calculated. Afterwards track candidates are formed by a combination of space-points. These track candidates then undergo the track-fitting procedure which yields track parameters with covariance at the closest point to the beam line. Good candidates are extrapolated to the TRT, whose hits then will be added.

xKalman++

xKalman++ is a reconstruction package for the ATLAS Inner Detector. It is controlled by xKalman which is also responsible for the reconstruction process and calls the sub-algorithms. At first a detector geometry description as well as a magnetic field map is produced. The reconstruction either extends over the full Inner Detector or focuses on a Region of Interest (RoI), which, for example, may be defined by a certain jet or lepton. After space points have been produced, the pattern recognition starts in the TRT (using a histogramming method). Primary tracks yield possible track candidates trajectories (incl. helix parameter and covariance matrix) which then are extrapolated to the precision tracker (just the other way round as iPatRec does). The clusters are compared and if enough clusters were hit uniquely, the track is kept. The tracks from TRT are extrapolated to the tracks found in the precision tracker by best track prolongation and drift-time information.

---

[4]STAtistical COmbination
[5]inner detector pattern recognition and track fitting

Moore

Moore[6][22] is a reconstruction package for tracks in the muon spectrometer. For the track fit itself it relies on iPatRec (see above). Moore executes the pattern recognition as follows: it begins with building the tracks in the x-y plane, which are supposed to be straight lines from the vertex, as in that plane the bending power of the toroidal magnetic field is negligible in the detector. At first the ϕ-coordinates are measured with the RPC, TGC and CSC ϕ-strips. These measurements then are merged into so called ϕ-segments.

In the RZ-plane ($\perp$ x-y plane), the tracks are bent and within each detector module (MDT, RPC, TGC and CSC) the tracks are approximated as straight lines ("crude" pattern recognition). Then the tracks in those muon spectrometer layers providing trigger signals are reconstructed. This is done by looping over all ϕ-segments and within those looping over the crude RZ-segments. In case a RZ-segment is near a ϕ-segment, so called "fine" RZ-segments are created. Now the hits which form ϕ-segments and fine RZ-segments are combined to a road using iPatTrack. In the last step, the final tracks which will be used for analyses, are reconstructed. The tracks produced by Moore are MooiPatTrack objects and their parameters are expressed at the first measured point within the muon system in terms of perigee parameters, which define the track at its point of closest approach to a reference point (usually the origin). Then, the hits from layers without trigger chambers are assigned to each road. Finally, energy loss and Coulomb scattering is taken into account.

Muonboy

The main points of the Muonboy pattern recognition are as follows [23]:

- identification of the region of activity (ROA) using the muon spectrometers triggers

- local straight track segments are reconstructed within each MDT chamber in the ROA

- combination of track segments to form a track candidate

- global track fit of the track candidate through the full system

The algorithm needs some input parameters, namely the drift time, the r-t relations (which describes the conversion from drift-time to drift-radius), a geometry description of the detector, alignment corrections and the magnetic field values. Muonboy

---

[6]Muon Object Oriented Reconstruction

treats multiple scattering and dead matter energy loss in calorimeters. Originally the algorithm was called Muonbox and was written in Fortran 77. A new version, called Muonboy, has been developed though, which is written in F90.

MuID

MuID[7][24] combines the information from the Muon Spectrometer (using Moore) with those from the Inner Detector (using iPatRec). The result are the track parameters of the identified and reconstructed muon at the interaction region. MuID consists of two parts:

- MuID standalone: this algorithm extrapolates the Muon Spectrometer tracks to the vertex in order to have a set of track parameters and a covariance matrix comparable to those from the Inner Detector. MuID propagates the Moore track through the magnetic field. Five additional parameters are used to express the mean energy loss in the calorimeter and to get the deflection and direction distribution. The energy loss is taken into account either via calorimeter energy deposition or as a parameterisation.

- MuID combined: a χ^2 using five degrees of freedom is formed from the difference of the five track parameters and their summed covariance is used to find a combination of muon spectrometer track and inner detector track. The parameters completely describe the track. There are several combinations of parameters, here the following is used: $\eta, \phi, \Delta\eta, \Delta\phi$ and r. The first pair of parameters describes the direction of the track in a certain point, e.g. the vertex, the second pair describes the deviation from this direction in a plane and the last parameter is the curvature r. If the magnetic field was unknown, there were two more parameters required, namely $\Delta\eta$ and $\Delta\phi$ in a plane perpendicular to the first one. This is done, if the χ^2 probability is above a certain threshold. Otherwise the combined fit uses only the muon track. Now the tracks are combined by using the information from those two subdetectors which were found and used separately by the standalone reconstruction. Satisfying matches to the Inner Detector resulting in a good combined fit are then treated as identified muons and stored.

STACO

As mentioned, STACO [25] uses the covariance matrices of two independent measurements for combination. The track reconstruction in the Inner Detector is performed by xKalman++ while the reconstruction in the Muon System is done by

---

[7]Muon IDentification

Muonboy (where the track parameters are expressed at the exit of the Inner Detector). Multiple scattering and energy loss fluctuations are treated in the covariance matrices, while energy loss corrections in the calorimeters are done in Muonboy using a momentum dependent parameterisation. Let P_1 and P_2 be two parameter vectors and C_1 and C_2 the covariance matrices of two tracks. Then the solution P of the following equation is the parameter vector of the combined track:

$$\left(C_1^{-1} + C_2^{-1}\right) \cdot P = C_1^{-1} \cdot P_1 + C_2^{-1} \cdot P_2 \qquad (4.4)$$

The covariance matrix is given by

$$C = \left(C_1^{-1} + C_2^{-1}\right)^{-1} \qquad (4.5)$$

and the corresponding χ^2 is given by

$$\chi^2 = (P - P_1)^T \cdot C_1^{-1} \cdot (P - P_1) + (P - P_2)^T \cdot C_2^{-1} \cdot (P - P_2) \qquad (4.6)$$

After combination the track is propagated to the beam line, where multiple scattering in the Inner Detector is included. Criteria for the track acceptance are good matching in the η-ϕ plane and the χ^2 being below a threshold.

4.2.5   Comparison Between the Algorithms

The reconstruction efficiency of MuID and STACO will be compared for several kinds of samples. Initially, the differences of the reconstruction will be shown using Single Muon Samples in a broad p_T range, namely from 10 GeV - 300 GeV. Differences in p_T, η and ϕ will be shown, as well as χ^2. Finally some implications of the muon reconstruction for physics samples like $Z/\gamma^* \to \mu\mu$ are described. A result of this examination is the insight, that both algorithms are quite mature and usable for most analyses. However both sometimes tend to misreconstruct muons which can lead to a fake signal.

Single Muon Samples

The Single Muon samples do contain only muons, one per event. They have been produced within the CSC[8] using Athena version 11.0.41 and cover a p_T range from 10 GeV to 300 GeV. For comparison of a reconstructed variable with the Monte Carlo Truth information the following definition will be used:

$$(\Delta p_T/p_T)^{\text{measured,MC}} = \frac{p_T^{\text{measured}} - p_T^{\text{MC}}}{p_T^{\text{MC}}}$$

$$\text{where } (\Delta p_T/p_T)^{\text{measured,MC}} > 0 \text{ if } p_T^{\text{measured}} > p_T^{\text{MC}} \qquad (4.7)$$

---

[8]Computing Service Challenge, see chapter 3

p_T [GeV]	inner σ	muon σ	combined σ
10	$2.41 \cdot 10^{-2}$	$1.24 \cdot 10^{-1}$	$2.48 \cdot 10^{-2}$
18	$2.51 \cdot 10^{-2}$	$8.57 \cdot 10^{-2}$	$2.42 \cdot 10^{-2}$
26	$2.61 \cdot 10^{-2}$	$7.52 \cdot 10^{-2}$	$2.46 \cdot 10^{-2}$
50	$3.04 \cdot 10^{-2}$	$4.65 \cdot 10^{-2}$	$2.69 \cdot 10^{-2}$
100	$4.89 \cdot 10^{-2}$	$4.42 \cdot 10^{-2}$	$3.15 \cdot 10^{-2}$
300	$1.20 \cdot 10^{-1}$	$4.64 \cdot 10^{-2}$	$4.76 \cdot 10^{-2}$

Table 4.1: σ deviation from $(\Delta p_T / p_T)$ for inner detector, muon spectrometer and combined reconstruction for MuID reconstruction

p_T [GeV]	inner σ	muon σ	combined σ
10	$2.44 \cdot 10^{-2}$	$1.15 \cdot 10^{-1}$	$2.38 \cdot 10^{-2}$
18	$2.51 \cdot 10^{-2}$	$7.31 \cdot 10^{-2}$	$2.33 \cdot 10^{-2}$
26	$2.61 \cdot 10^{-2}$	$5.17 \cdot 10^{-2}$	$2.37 \cdot 10^{-2}$
50	$3.04 \cdot 10^{-2}$	$4.03 \cdot 10^{-2}$	$2.55 \cdot 10^{-2}$
100	$4.56 \cdot 10^{-2}$	$3.73 \cdot 10^{-2}$	$3.01 \cdot 10^{-2}$
300	$1.09 \cdot 10^{-1}$	$4.89 \cdot 10^{-2}$	$4.28 \cdot 10^{-2}$

Table 4.2: σ deviation from $(\Delta p_T / p_T)$ for inner detector, muon spectrometer and combined reconstruction for STACO reconstruction

This thesis is based upon the use of Monte Carlo samples, but in principle each sample includes two types of Monte Carlo data. The first is the Truth information, this basically is the information from the Monte Carlo generator, while the second one is the simulated information. This is the Monte Carlo information from the generator but reconstructed with the detector simulation. By comparing the Monte Carlo Truth with the Monte Carlo reconstructed values one can achieve information about the reconstruction process.

The parameter σ is determined from a Gaussian fit and reflects the width of the (fitted) curve while μ stands for the mean value:

$$f(x, \mu, \sigma) = \frac{1}{\sigma\sqrt{2\pi}} e^{\left(-\frac{(x-\mu)^2}{2\sigma^2}\right)} \tag{4.8}$$

From the tables 4.1 and 4.2 and the corresponding figures (4.7,4.9) one can see, that the deviation from the Monte Carlo Truth information depends on the p_T. For lower p_Ts the Gaussian width of the combined reconstruction resembles the inner
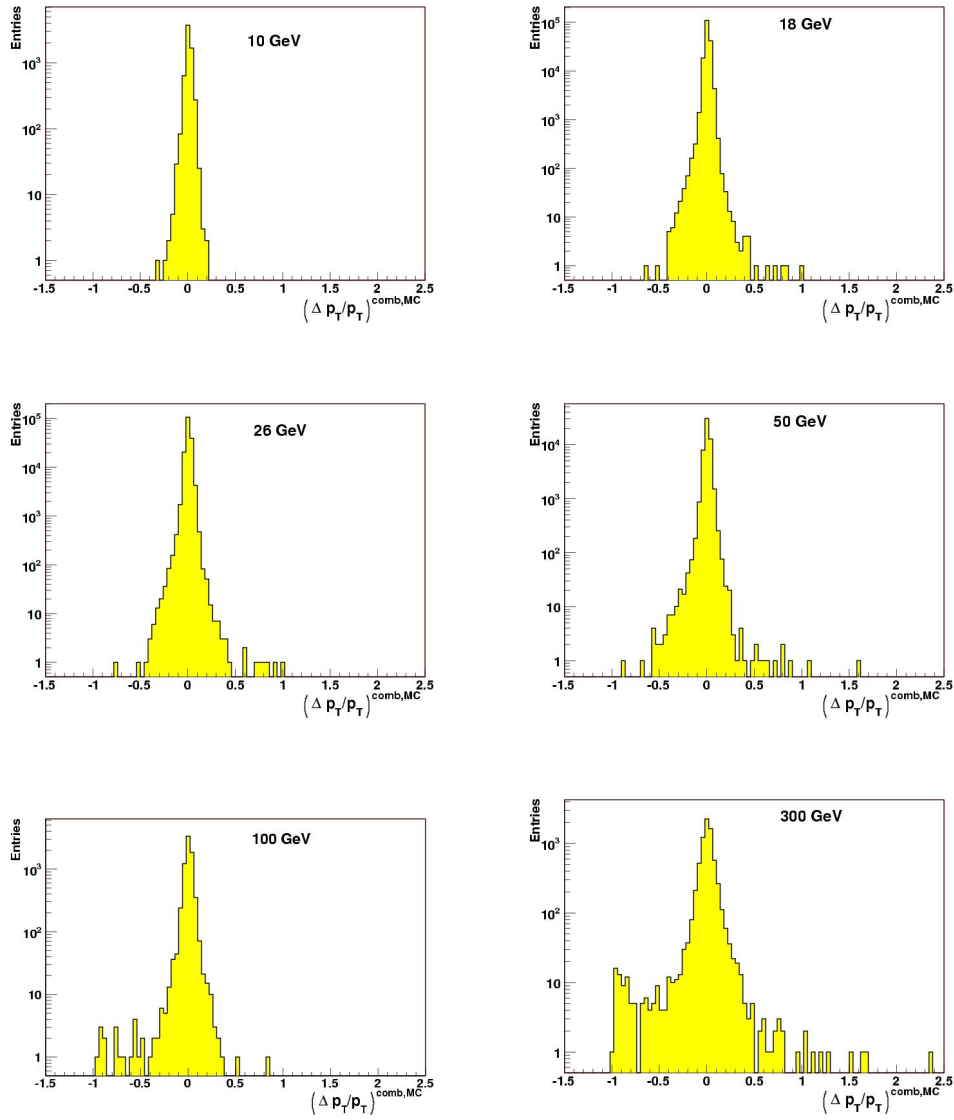
Figure 4.7: $(\Delta p_T/p_T)^{comb,MC}$ for 10-300 GeV using MuID reconstruction. The single muon samples have fixed p_T values.
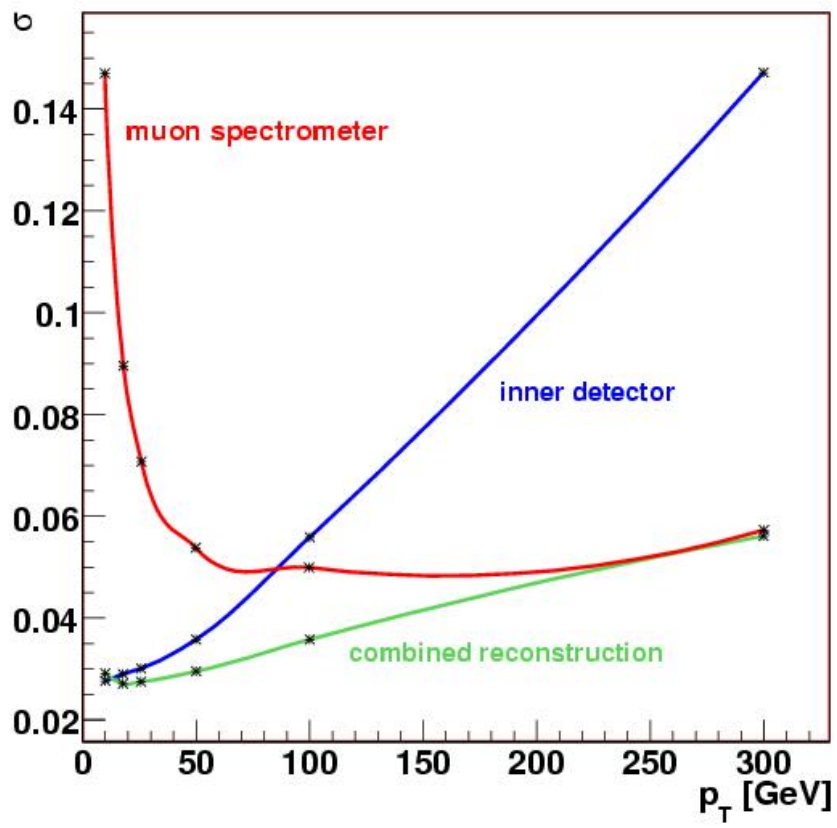
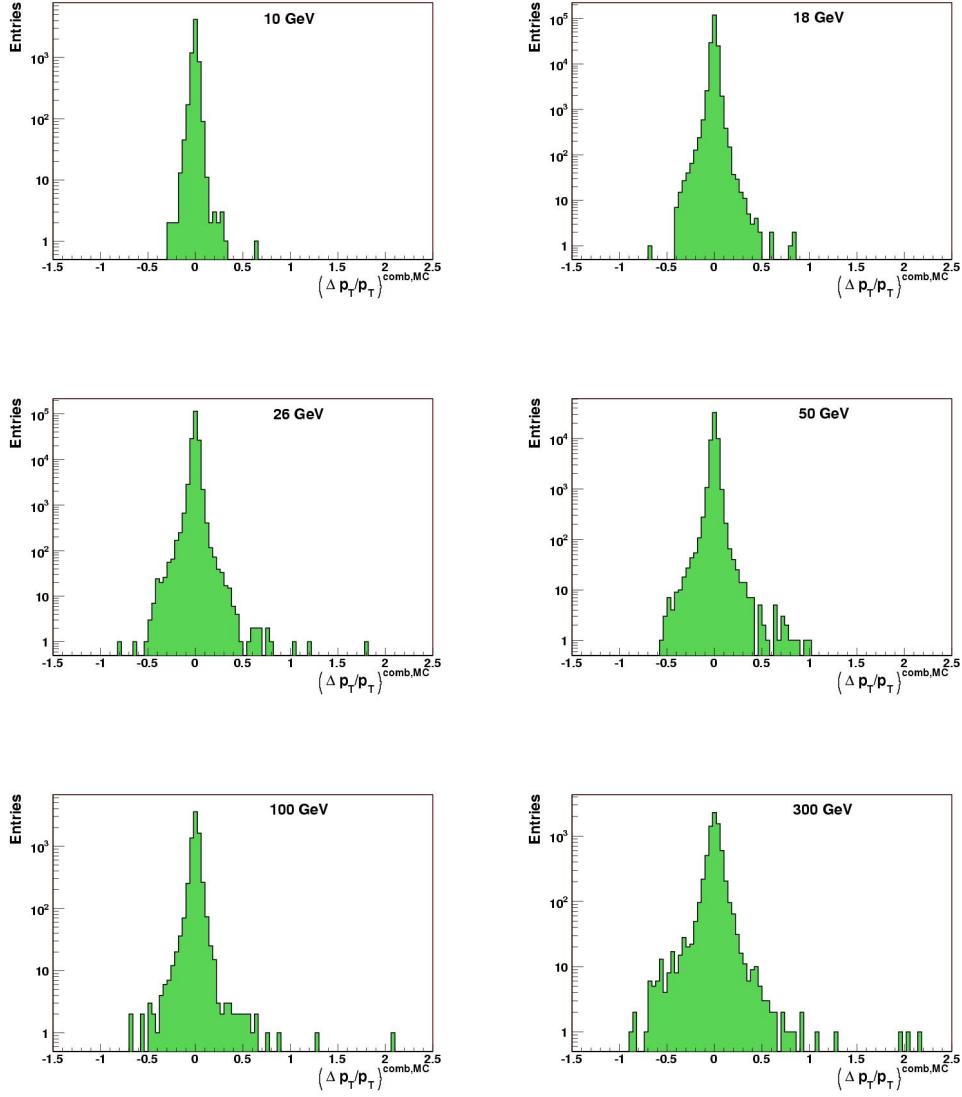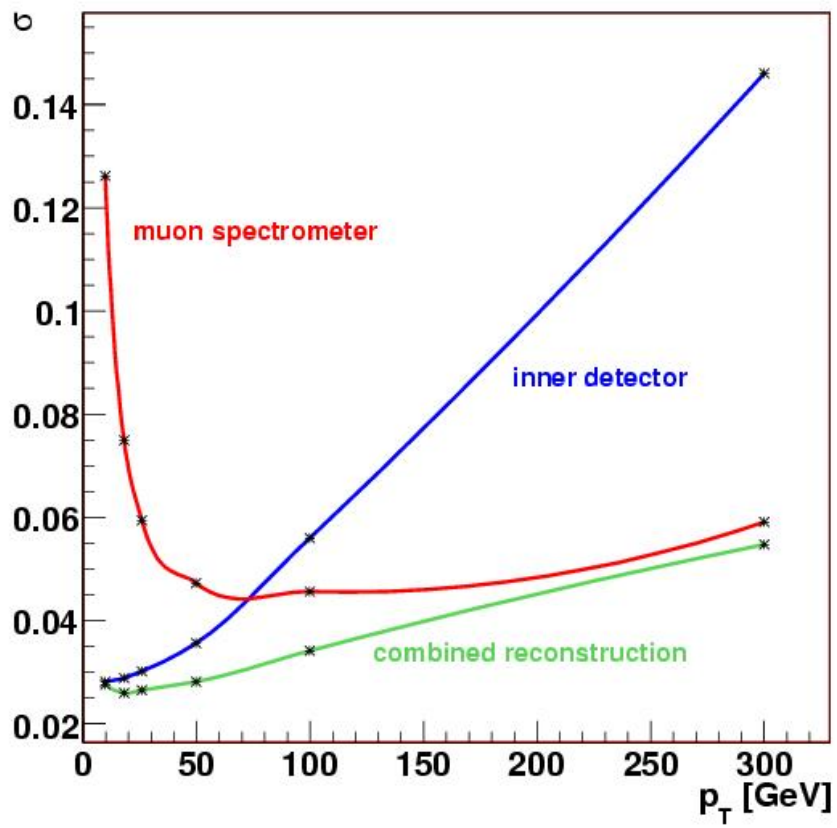Figure 4.8: σ for MuID reconstruction for 10-300 GeV

Figure 4.9: $(\Delta p_T/p_T)^{comb,MC}$ for 10-300 GeV using STACO reconstruction. The single muon samples have fixed p_T values.
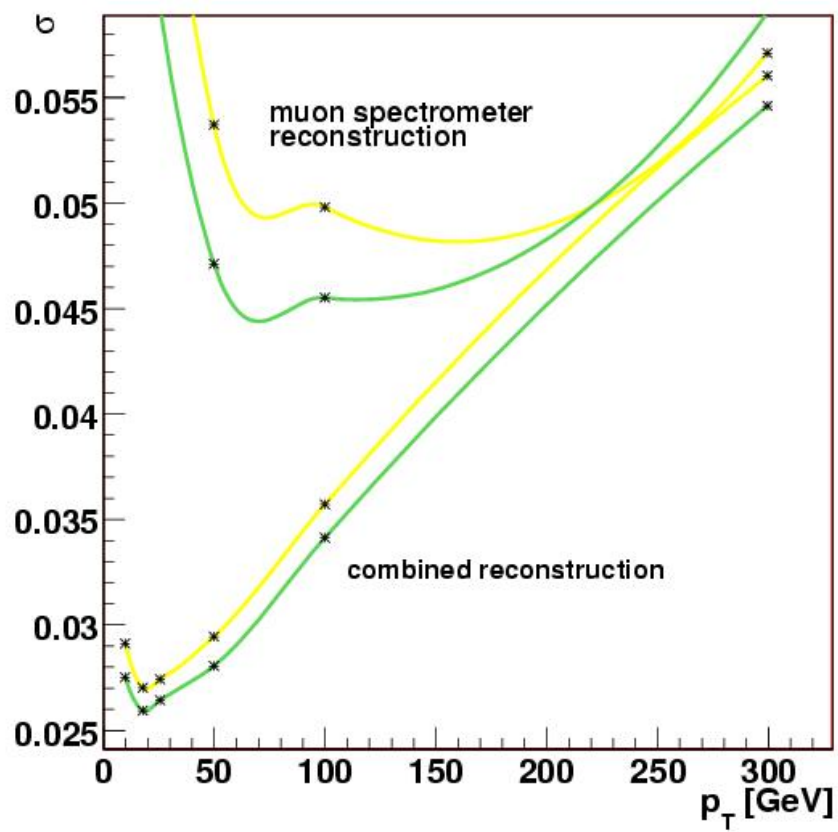
Figure 4.10: σ for STACO reconstruction for 10-300 GeV

Figure 4.11: σ for STACO and MuID reconstruction for 10-300 GeV. MuID curves are marked yellow, STACO curves are marked green.

detector standalone reconstruction while for the highest bin (300 GeV) the width resembles the muon standalone reconstruction. This is expected as for higher p_Ts the muon standalone reconstruction is better than the inner detector standalone reconstruction. Using MuID the reconstruction shows some unexpected behaviour. For 10 GeV the σ of the inner reconstruction is smaller than the σ of combined reconstruction. A reason could be that the weighting of the muon reconstruction in the combination algorithm is slightly too large. This could lead to a higher σ for combined reconstruction, the deviation is very small, though. For the 300 GeV sample there are many muons in the non-Gaussian tail of the muon standalone reconstruction. They are not included in the fit, hence the σ is slightly smaller for the standalone reconstruction. When applying a cut on the central region of the reconstruction, requiring

$$(\Delta p_T/p_T)^{comb,MC} < 0.05 \quad \wedge \quad (\Delta p_T/p_T)^{muon,MC} < 0.05, \tag{4.9}$$

after fitting a Gaussian the σ of combined reconstruction is smaller than the σ of muon standalone reconstruction. This is the expected behaviour of the reconstruction algorithm.

The resolution of the Muon spectrometer standalone reconstruction at first improves, with an optimum at approximately 60 GeV. Then it decreases, also monotonously but with a much smaller slope. The resolution of the combination of both methods in general yields the best resolution over the studied p_T-range. The resolutions are shown in figure 4.8 and in figure 4.10. As a result, the weight of inner detector and muon spectrometer reconstruction contributing to the combination depends on the p_T. This is also the expected behaviour, as for higher p_Ts the track of the particle is less bent which results in imprecise reconstruction in the Inner Detector, mainly because of the relatively small dimensions of the Inner Detector. The toroidal magnetic field bends the trajectory over a larger distance and allows a more precise measurement in the Muon Spectrometer. Additionally, the measurement in the muon spectrometer takes place after the particle traversed the calorimeters which leads to a loss of energy. This effect is more distinct for lower p_Ts.

Sometimes the reconstruction or combination fails, producing an overestimated (or underestimated) p_T signal. In that case the use of either Inner Detector or muon spectrometer reconstruction might be preferred over the combined reconstruction. This analysis deals with overestimated p_Ts as these might fake a leptoquark signal.

Table 4.3 shows the relative number of particles outside of $3\tilde{\sigma}$ for the three reconstruction methods (inner detector, muon spectrometer and combined reconstruction) for MuID combined as well as STACO reconstruction. This is done for the whole
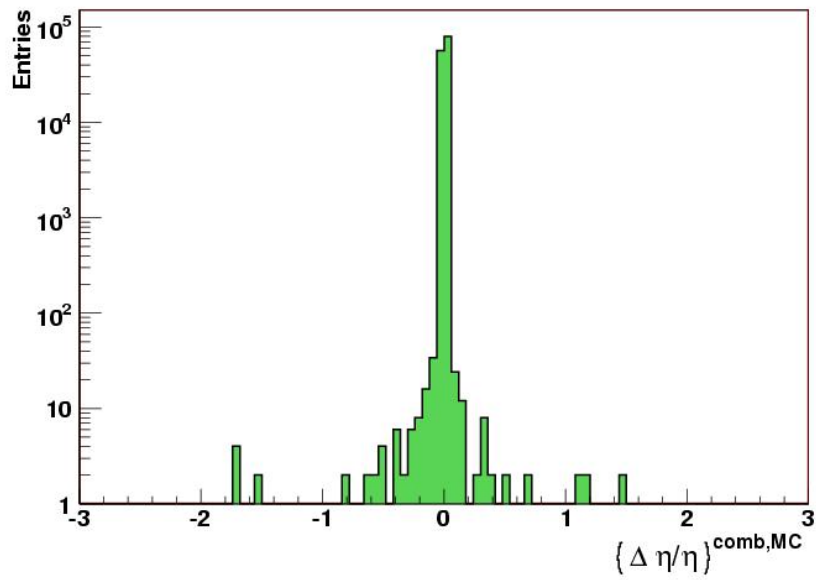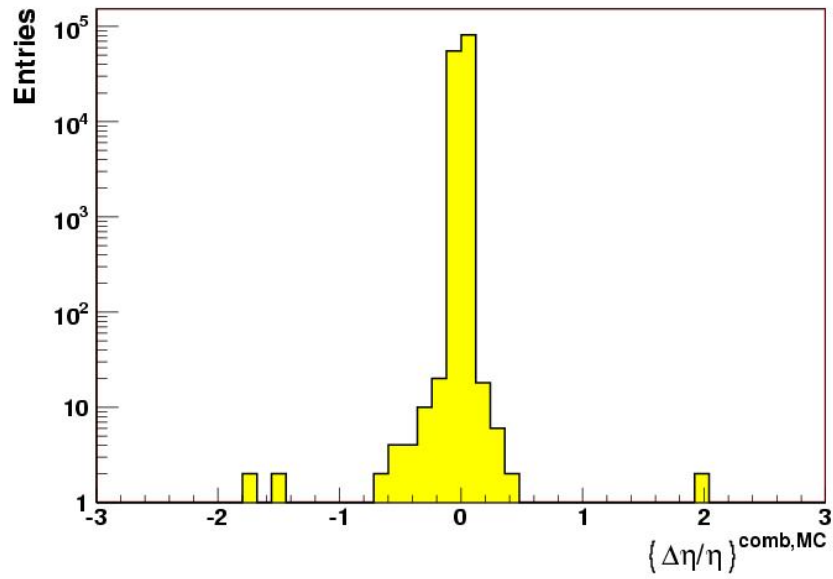
Figure 4.12: $(\Delta\eta/\eta)^{comb,MC}$ for MuID reconstruction (yellow) and STACO recon-
struction (green), both for 50 GeV

p_T [GeV]	10	18	26	50	100	300
$3\tilde{\sigma}_i / \cdot 10^{-2}$	7.62	7.98	8.64	10.89	16.62	42.6
MuID inner	$5.58 \cdot 10^{-3}$	$7.92 \cdot 10^{-3}$	0.012	0.013	0.028	0.024
STACO inner	$6.26 \cdot 10^{-3}$	$8.14 \cdot 10^{-3}$	0.012	0.012	0.027	0.044
$3\tilde{\sigma}_c / \cdot 10^{-2}$	7.74	7.35	7.52	8.43	10.55	16.59
MuID comb	$4.65 \cdot 10^{-3}$	$3.37 \cdot 10^{-3}$	$3.59 \cdot 10^{-3}$	$7.41 \cdot 10^{-3}$	$7.49 \cdot 10^{-3}$	0.026
STACO comb	$3.51 \cdot 10^{-3}$	$3.64 \cdot 10^{-3}$	$4.18 \cdot 10^{-3}$	$7.38 \cdot 10^{-3}$	$9.23 \cdot 10^{-3}$	0.025
$3\tilde{\sigma}_m / \cdot 10^{-2}$	34.73	22.44	18.21	14.54	13.97	17.03
MuID muon	0.023	$6.79 \cdot 10^{-3}$	0.010	0.022	0.042	0.067
STACO muon	$2.75 \cdot 10^{-3}$	$4.20 \cdot 10^{-3}$	$6.45 \cdot 10^{-3}$	0.012	0.025	0.049

Table 4.3: This table shows the fraction of particles outside of $3\tilde{\sigma}$ for the p_T-spectrum investigated in this analysis

p_T spectrum investigated in this analysis.

$$\tilde{\sigma} = \frac{\sigma^{\text{MuID}} + \sigma^{\text{STACO}}}{2} \tag{4.10}$$

From the table some conclusions can be drawn. For lower p_Ts, the width of the combined reconstruction resembles the width of the inner detector. This means that in this area the combination mainly uses the information from the inner detector. On the other side, for higher p_Ts, the width of the combined reconstruction resembles the one of the muon spectrometer. So in this area a main part of the combined reconstruction uses the muon spectrometer.

Another interesting detail is that even if the width of the muon spectrometer and the combined reconstruction are similar for high p_T, the number of particles in the tail (meaning the p_T estimation was too high) from muon standalone reconstruction is much higher than for the combined reconstruction. The consequence is, that in general one should not only use the inner detector information for lower p_Ts and muon standalone reconstruction for higher p_Ts, but a combination of both. This yields a relatively low number of particles in the tail. Nonetheless in some cases the use of a standalone reconstruction, either inner detector or muon spectrometer is better to reduce the number of particles in the tail of the distribution. Details will be discussed in chapter 5, for the moment the reader is referred to table 4.5, which shows the relative number of muons in the area greater than $\left\langle (\Delta p_T/p_T)^{\text{measured,MC}} \right\rangle +$ $3\hat{\sigma}$ without $|\eta|$ cut and with requiring $|\eta| \leq 2$. From the table it can be seen that, after applying the cut, the number of particles in the tail reduces compared to the distribution with no geometrical $|\eta|$ cut. This is valid for both, the inner detector standalone as well as the combined reconstruction. Furthermore in the first case the number of particles in the tail is larger for the inner detector standalone reconstruction than for the combined reconstruction – although the width of the standalone reconstruction is broader and therefore could contain more particles. In the latter case the behaviour is the other way round, at least for the p_T range lower than 10 GeV. As expected, the inner detector has the dominant weight in the combination.

Standard Model: $Z/\gamma^* \rightarrow \mu\mu$ Sample

In this chapter the reconstruction for a $Z/\gamma^* \rightarrow \mu\mu$ sample is analysed. Figure 4.13 shows $(\Delta p_T/p_T)^{comb,MC}$ using MuID and the same using STACO. In both cases some muons have been misreconstructed, but for the reconstruction with MuID there are a few more muons in the tail. The performance of the algorithms will be compared again in chapter 5, then applying the yet to be introduced selection method for the reconstruction.

$p_T[GeV]$	without cuts			geometrical cut: $\lvert \eta \rvert \leq 2$		
	$3\tilde{\sigma}_i \cdot 10^2$	$3\tilde{\sigma}_c \cdot 10^2$	$3\hat{\sigma}^0 \cdot 10^2$	$3\tilde{\sigma}_i \cdot 10^2$	$3\tilde{\sigma}_c \cdot 10^2$	$3\hat{\sigma}^1 \cdot 10^2$
10	7.62	7.74	7.68	6.77	6.99	6.88
18	7.98	7.35	7.67	7.05	6.87	6.96
26	8.64	7.52	8.08	7.44	7.04	7.24
50	10.89	8.43	9.66	9.12	7.92	8.52
100	16.62	10.55	13.59	14.04	10.22	12.13
300	42.6	16.59	29.60	35.07	16.53	25.80

Table 4.4: This table lists the σ of Gaussian fits to the p_T distribution. In the left part of the table the σs have been calculated with no constraints and in the right part the particles tracks are constrained within $\eta \leq 2$. STACO reconstruction has been used.

Figure 4.14 shows the reconstructed dimuonmass for both, MuID reconstruction and STACO reconstruction

$$M_{\mu\mu}^2 = \left(\sum_{i=1}^{2} E_i \right)^2 - \left(\sum_{i=1}^{2} \vec{p}_i \right)^2 \geq 0 \qquad (4.11)$$

which in both cases coincides the best experimental value [19] of the Z bosons mass $M_Z = 91.19$ GeV within the uncertainties. For both reconstruction methods, MuID and STACO, the number of particles in the tail resemble.

Figure 4.15 shows the distribution of the degrees of freedom from χ^2 for MuID. A similar plot for STACO would have one sharp peak at 5 degrees of freedom, as this is a property of the statistical combination algorithm (see 4.2.4). As will be explained further in chapter 5, the number of degrees of freedom does not necessarily influence the quality of the fit. If there are less degrees of freedom, in general the particles trajectory has a high η and traverses the detector in the end-cap region. In that area the number of subdetectors is reduced compared to the barrel region.

		without constraints			constraint: $|\eta| \leq 2$	
$p_T[GeV]$	$3\hat{\sigma}^0 \cdot 10^2$	STACO inner	STACO comb	$3\hat{\sigma}^1 \cdot 10^2$	STACO inner	STACO comb
10	7.68	$6.26 \cdot 10^{-3}$	$3.51 \cdot 10^{-3}$	6.88	$6.03 \cdot 10^{-3}$	$2.21 \cdot 10^{-3}$
18	7.67	$8.14 \cdot 10^{-3}$	$3.64 \cdot 10^{-3}$	6.96	$1.15 \cdot 10^{-3}$	$2.59 \cdot 10^{-3}$
26	8.08	$12.13 \cdot 10^{-3}$	$4.18 \cdot 10^{-3}$	7.24	$1.05 \cdot 10^{-3}$	$3.23 \cdot 10^{-3}$
50	9.66	0.028	$7.38 \cdot 10^{-3}$	8.52	$4.53 \cdot 10^{-3}$	$4.77 \cdot 10^{-3}$
100	13.59	0.043	$9.23 \cdot 10^{-3}$	12.13	0.012	$5.23 \cdot 10^{-3}$
300	29.60	0.081	0.010	25.8	0.057	0.012

Table 4.5: relative number of particles outside $\left\langle (\Delta p_T/p_T)^{\text{measured,MC}} \right\rangle + 3\hat{\sigma}$ without constraints (left) and requiring $|\eta| \leq 2$ (right). STACO reconstruction has been used.
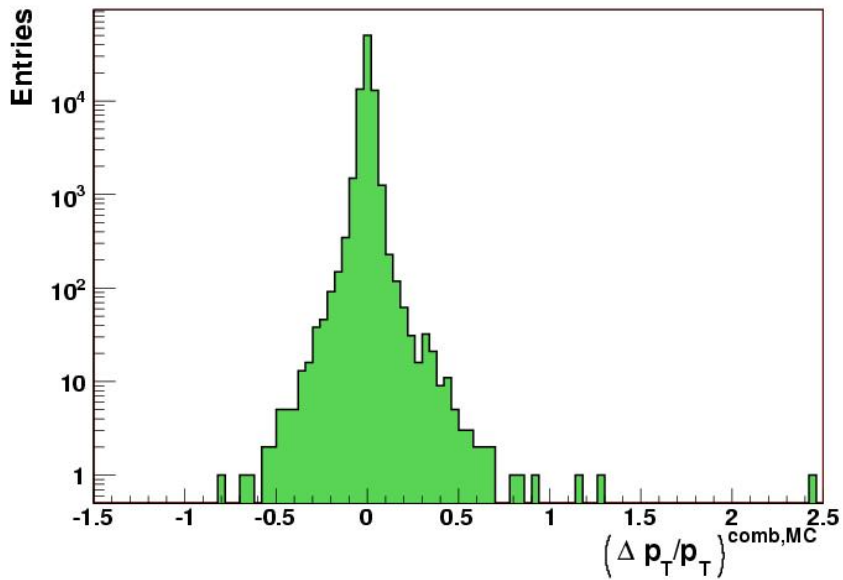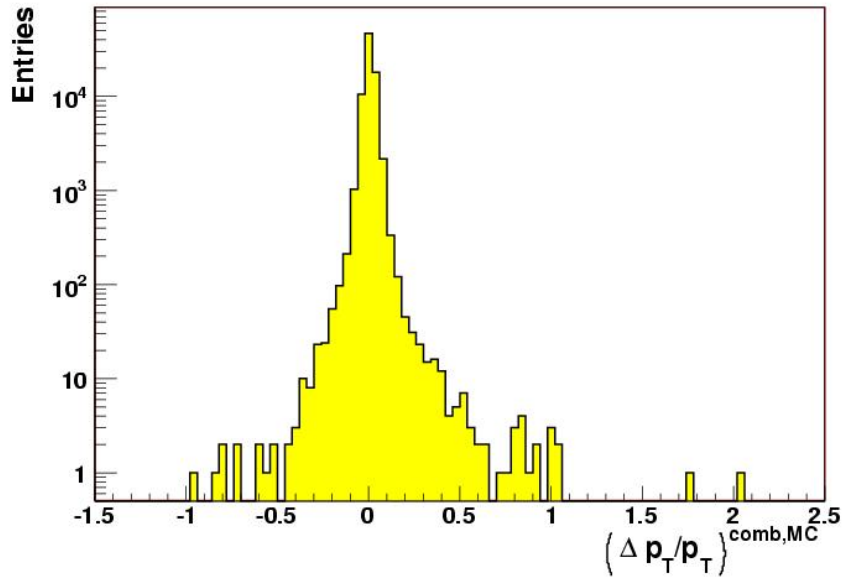
Figure 4.13: $(\Delta p_T/p_T)^{comb,MC}$ for MuID reconstruction (yellow) and STACO reconstruction (green) for the Standard Model $Z/\gamma^* \to \mu\mu$ sample.
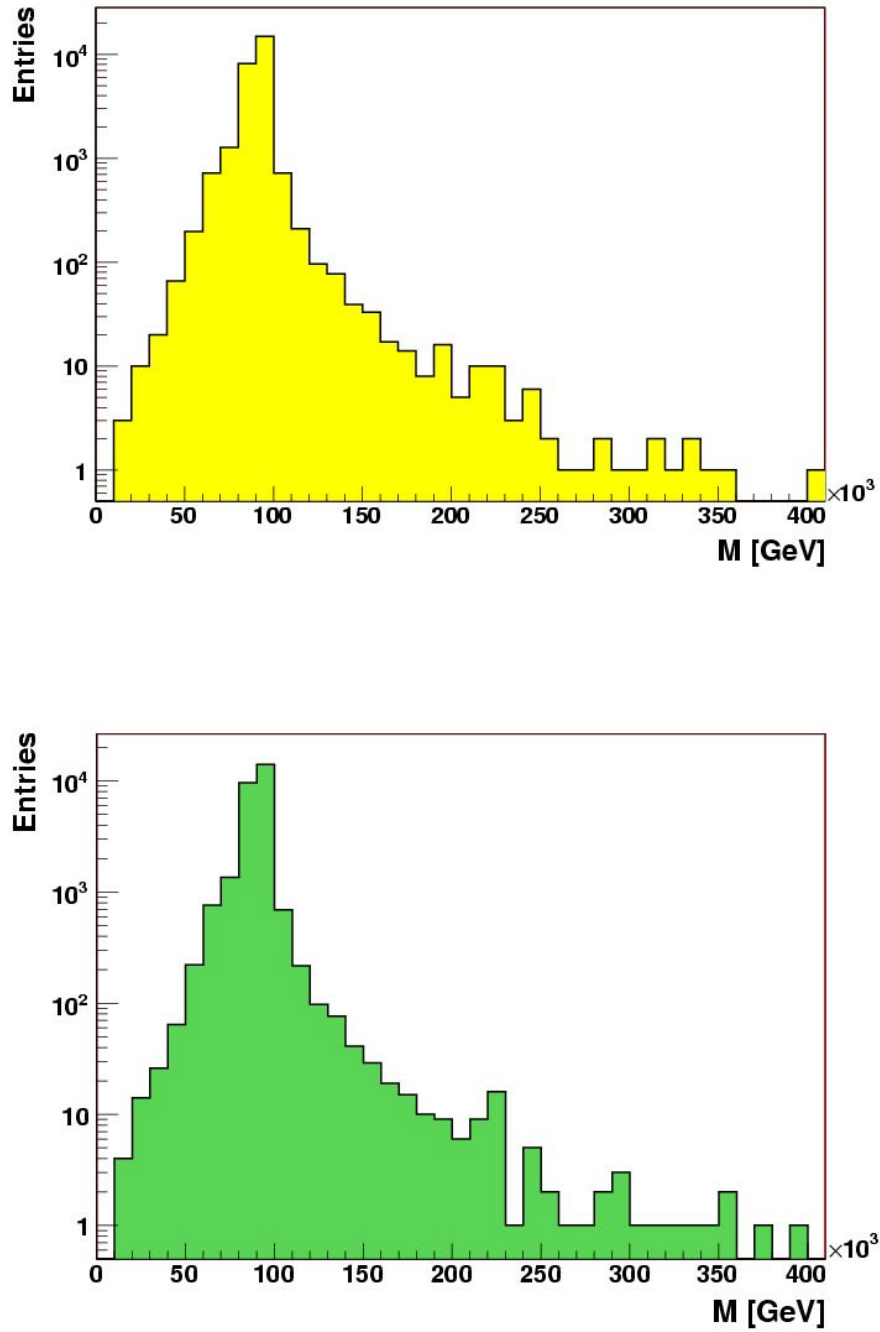
Figure 4.14: Z-Peak for MuID reconstruction (yellow) and STACO reconstruction (green).
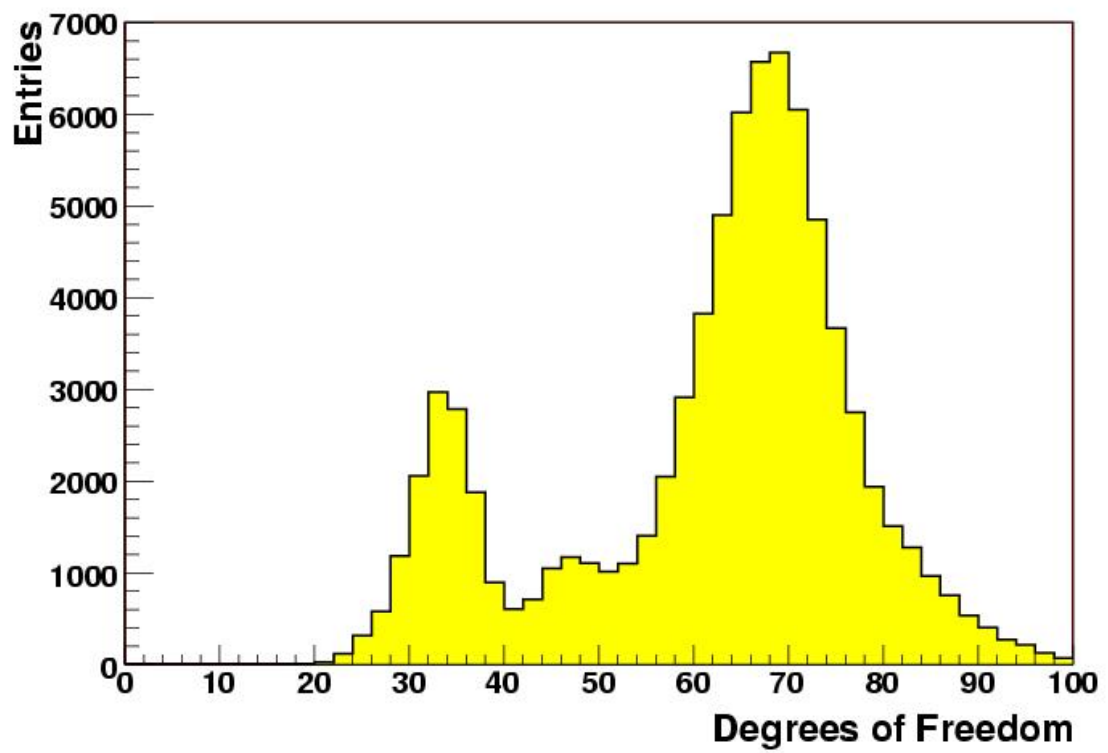
Figure 4.15: Number of degrees of freedom for MuID reconstruction

Beyond Standard Model: Leptoquark Sample

The leptoquark sample produced in Munich, has approximately 1000 events. The low statistics only allows limited conclusions from the following plots. The figure 4.16 shows a comparison between the combined reconstruction and Monte Carlo Truth information using the MuID and STACO algorithms. The MuID reconstruction produces less tails in the muon reconstruction than STACO does. Compared to the single muons it is the inverse behaviour, as for the single muons the MuID reconstruction tends to produce more tails for the combined reconstruction, but contrarily for the inner detector standalone this is not true (see 4.16). The comparison of the inner detector standalone reconstruction is basically the comparison of xKalman and iPatRec. Interestingly if using combined reconstruction for the single muons as well as for the leptoquarks, the number of particles in the tail of the p_T reconstruction is larger for STACO than for MuID reconstruction, while for the $Z/\gamma^* \to \mu\mu$ sample the opposite is true, see figure 4.13.
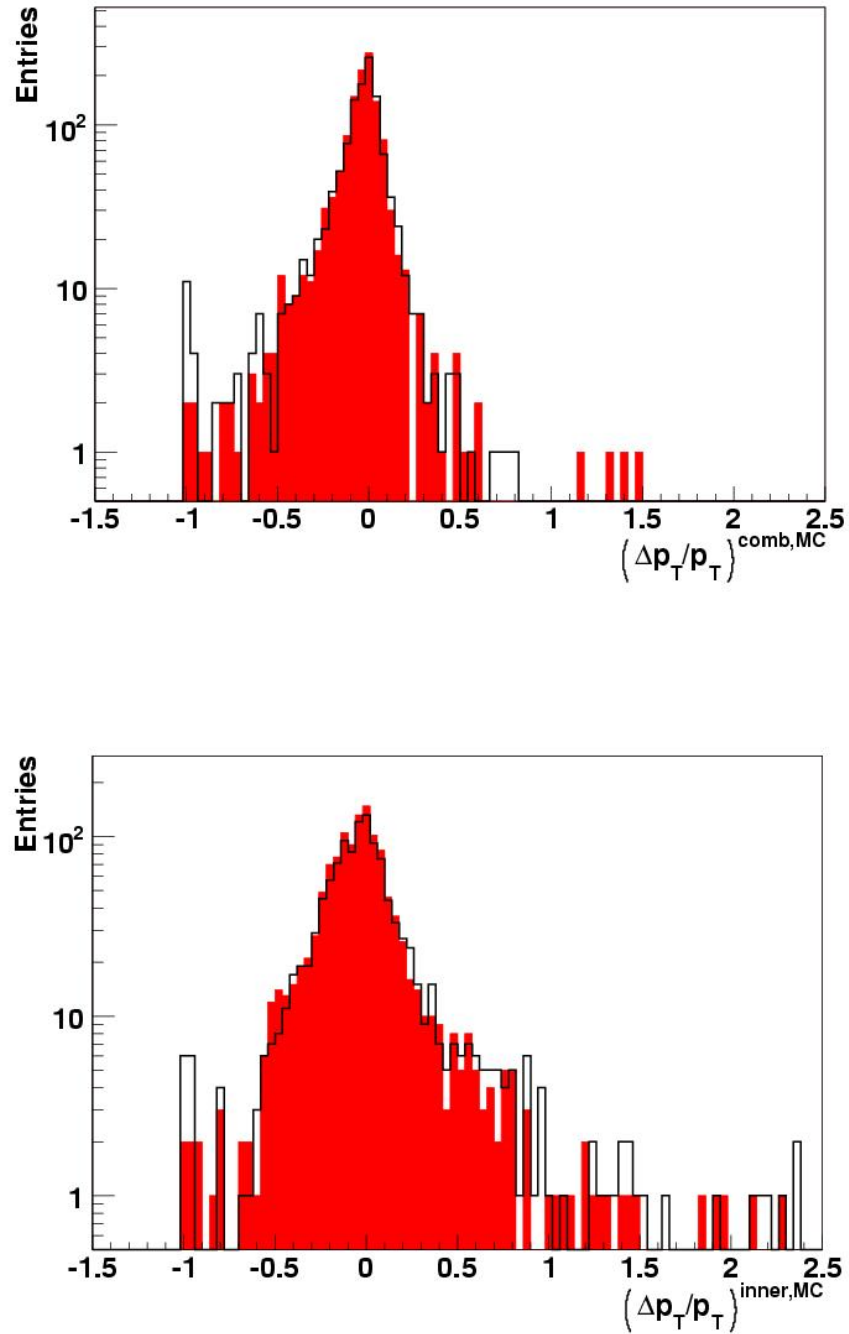
Figure 4.16: This plot shows a comparison between the combined muon reconstruction using MuID (black) and STACO (red) and the same for inner detector standalone reconstruction. The leptoquark mass of this sample is 1200 GeV.

5 The Simulation Study and Analysis

In Chapter 4.2 the reconstruction procedure for particles detected within the ATLAS detector has been described. The different reconstruction methods were introduced, as well as a comparison between the different algorithms. In anticipation and as motivation of this chapter the influence of a geometrical cut on the p_T-reconstruction was mentioned. The aim of this chapter is the detailed study of the muon reconstruction and the subsequent optimal classification of muons in to categories. Within each of these categories a different reconstruction is used in order to reduce the number of muons for which the p_T is significantly overestimated. These misreconstructed muons could lead to fake signals (e.g. for leptoquarks) in a background sample. As the current statistics in physics and background samples is low a weighting method will be introduced, which allows – independently from background samples – to make predictions about the reconstruction. This interval-method will then be applied to physics samples.

5.1 Investigation of the Track Quality

As a first step, the track's χ^2/DoF[1] distribution will be discussed. For a short introduction to the estimation of the fit quality the reader is referred to Appendix A. The value of χ^2 standalone is not too helpful, because it depends on the number of degrees of freedom. To resolve this dependence the χ^2 is divided by the degrees of freedom. For the STACO algorithm the DoF always equals five, as this is an attribute of the algorithm, for the MuID reconstruction the DoF ranges over a broad spectrum (as explained in chapter 4.2.4). The distribution of the degrees of freedom from MuID is shown in figure 5.1. The figure also clearly shows that for $|\eta| < 2$ and for $|\eta| \geq 2$ the number of degrees of freedom differs. For the more central region the distribution peaks around 69 while at the outer region there are two peaks, one at

---

[1]DoF stands for degrees of freedom
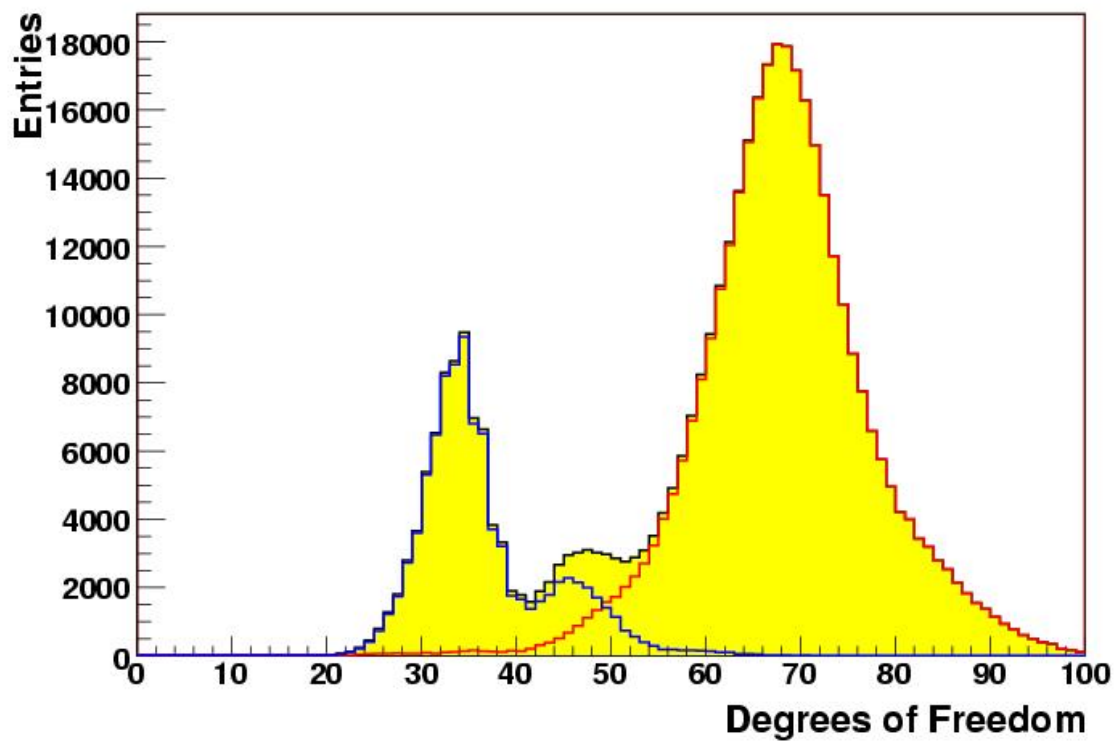
Figure 5.1: Distribution of the degrees of freedom using Single muon samples with MuID (yellow). The blue curve shows the distribution of DoF for $|\eta| > 2$ and the red curve the DoF distribution for $|\eta| \leq 2$.
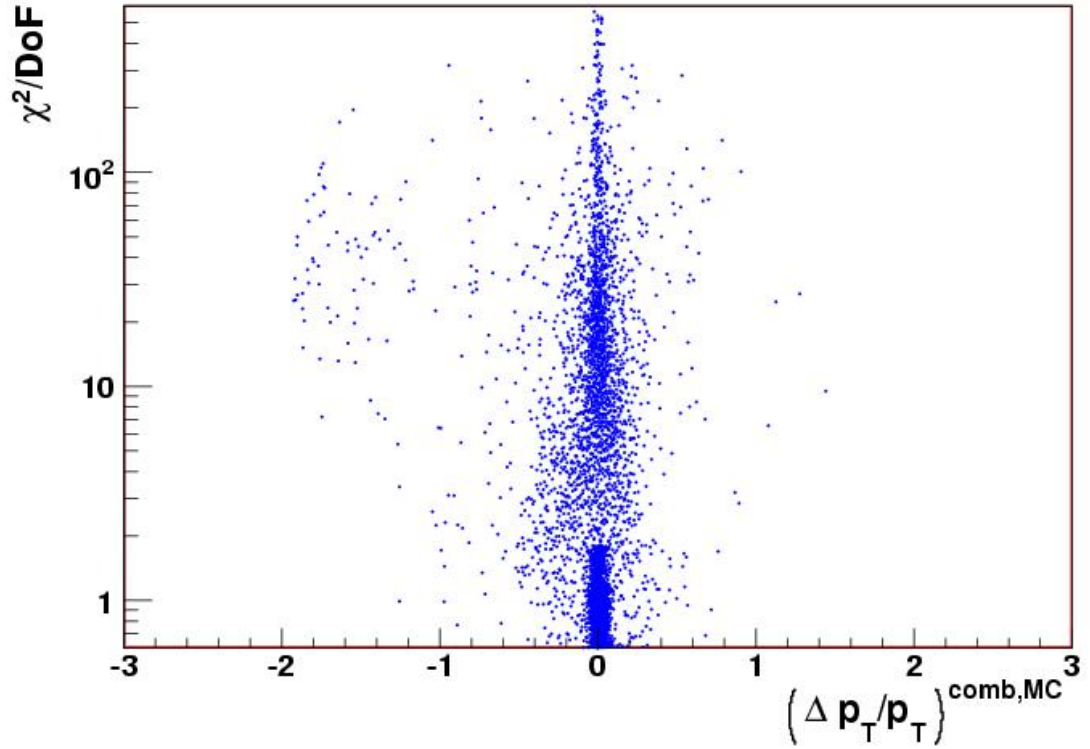
Figure 5.2: Distribution of $(\Delta p_T/p_T)^{comb,MC}$ versus χ^2/DoF

35 and the other at 46. The reason is that for the central region more subdetectors are hit which results in more degrees of freedom. In other words, a low number of degrees of freedom can not necessarily be ascribed to problems in the reconstruction. Especially in the region $\eta > 2$ the subdetectors produce less hits because of hardware properties. So the degrees of freedom depend on the direction of the particle but the track quality not necessarily depends on the degrees of freedom. This motivates the use of the parameter χ^2/DoF as a quantity for the track quality. For example in figure 5.2 the difference of combined reconstruction and Monte Carlo information is plotted versus χ^2/DoF.

From this plot follows that:

- even if p_T^{comb} and p_T^{MC} (nearly) coincide, there is a significant number of particles where χ^2/DoF is large.

- a number of particles have a reconstructed p_T which has been falsely reconstructed but the χ^2/DoF predicts a "good" track.

This means, that a further investigation of the χ^2/DoF could lead to a selection criterion in order to reduce the number of particles with overestimated p_T. Figure 5.3 shows a comparison between $(\Delta p_T/p_T)^{comb,MC}$ as well as for $(\Delta p_T/p_T)^{inner,MC}$ for $\chi^2/\text{DoF} > 1.5$ and $\chi^2/\text{DoF} \leq 1.5$. The upper plot ($\chi^2/\text{DoF} \leq 1.5$) indicates, that – as expected – the combined fit gives the better resolution, however for $\chi^2/\text{DoF} > 1.5$ (lower plot) the combined fit yields large tails. For example the number of particles with $(\Delta p_T/p_T)^{comb,MC} > 0.5$ reduces from 40 to 0 if applying the cut for χ^2/DoF. But one also sees, that most of the track with large χ^2/DoF are still well reconstructed. The number of particles thrown away would equal approximately 4% of the total number of particles. Throwing away muons with large χ^2 would reduce the statistics which might – depending on the details of the specific search – outweigh the advantage of a reduced background. There is also the risk of producing statistical errors. There might be a discrepancy between simulated and real data. It is possible, that not 4%, but much more events are thrown away due to a larger χ^2 in the real data. As another source of statistical error, it is possible that the events with particles having a large χ^2 are a certain, unidentified class of events. For example, the muon was not isolated or there are other particles. The aim of this study is therefore to reduce the number of misreconstructed muons without throwing away any of them by optimising the selection of the algorithm in different regions of phase space. In this case this can be achieved by selecting the combined fit for $\chi^2/\mbox{DoF} \leq 1.5$ and the inner detector standalone reconstruction for $\chi^2/\text{DoF} > 1.5$. The figure 5.4 shows the results of this selection. The blue curve shows the inner detector standalone reconstruction while the red curve shows the combined reconstruction. It has to be stressed, that no events are thrown away, but the best reconstruction available is selected instead. The selection of the inner detector reconstruction for $\chi^2/\text{DoF} > 1.5$ and combined reconstruction for $\chi^2/\text{DoF} \leq 1.5$ is the best choice: it reduces the number of particles in the tail drastically, keeps the distribution narrow and no event is thrown away (figure 5.4).

5.2   Selection of the Optimal Parameters

Hitherto the reconstruction has been compared to Monte Carlo Truth information. For a first insight and conclusions comparisons with the Truth information are quite
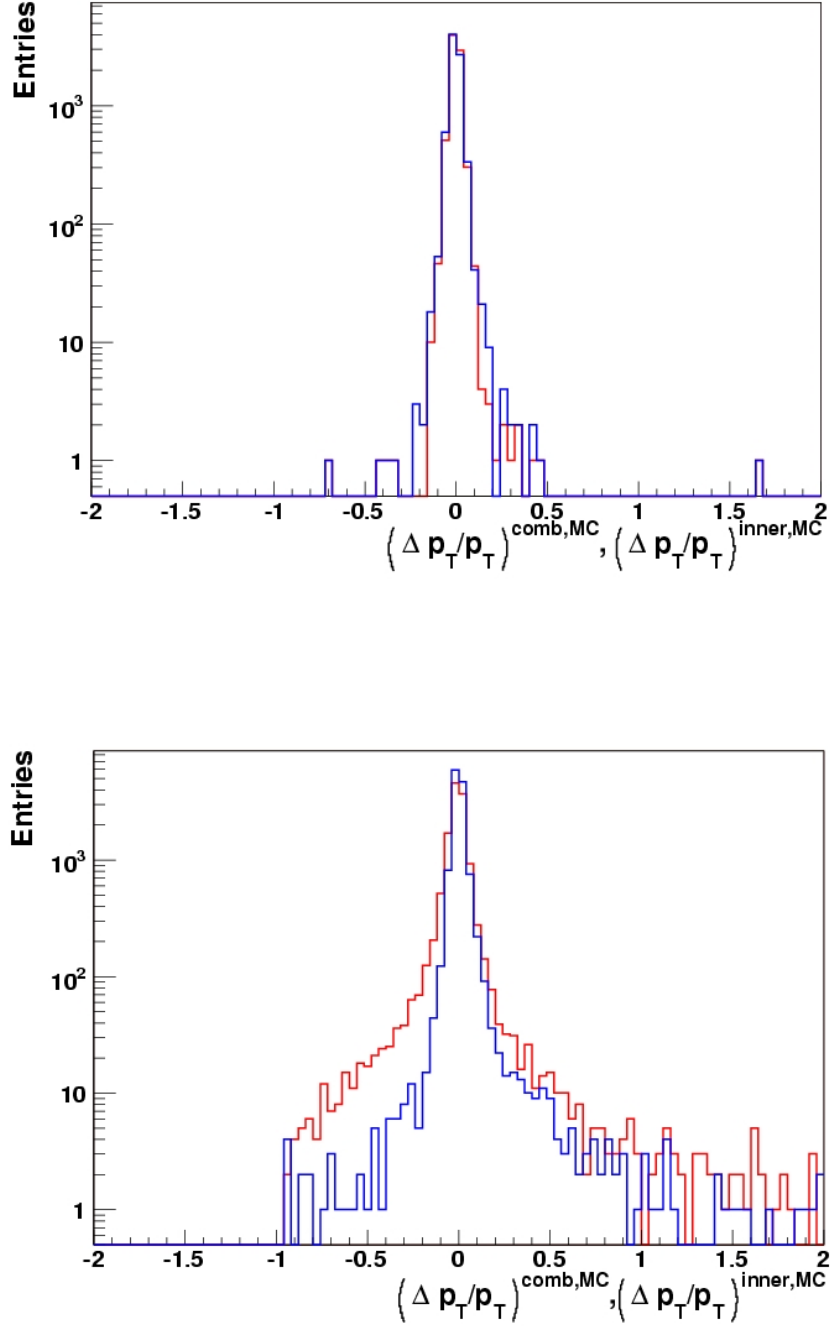
Figure 5.3: Comparison of combined and inner detector reconstruction with Monte Carlo for $\chi^2/\text{DoF} \leq 1.5$ (upper plot) and $\chi^2/\text{DoF} > 1.5$ (lower plot). In both plots the red curves show $(\Delta p_T/p_T)^{comb,MC}$ and the blue curves show $(\Delta p_T/p_T)^{inner,MC}$. The plots have been created with a $Z/\gamma^* \rightarrow \mu\mu$ sample.
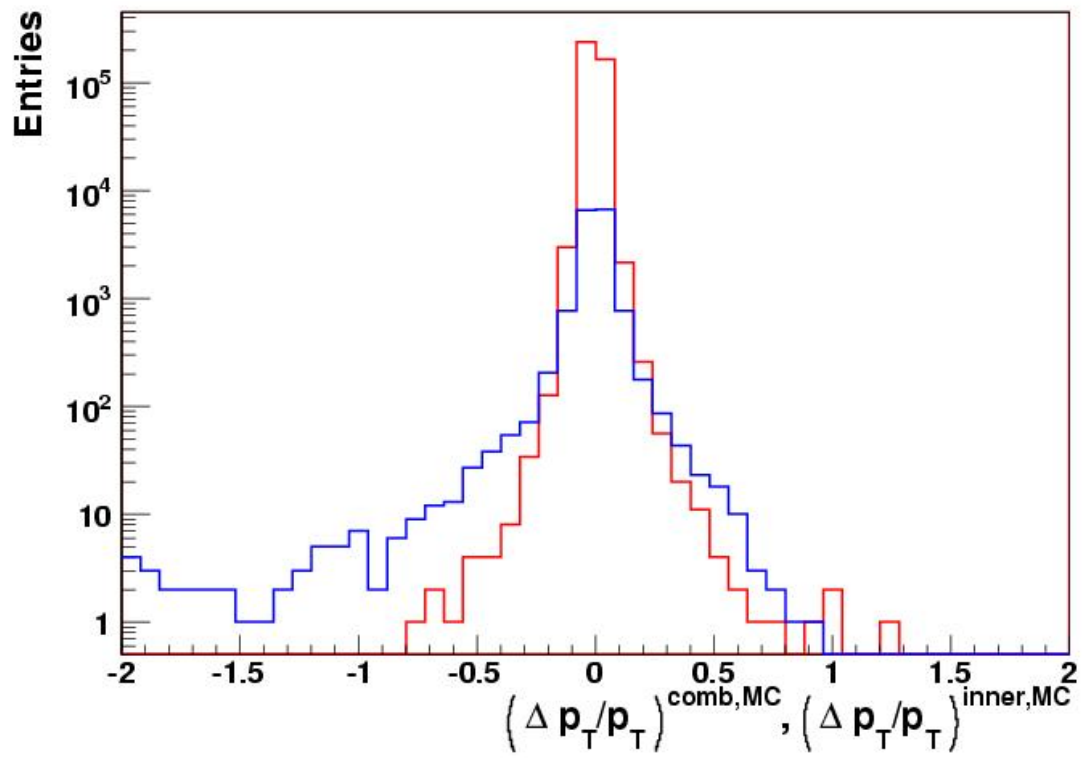
Figure 5.4: The plot shows the result of the χ^2/DoF selection. If $\chi^2/\mathrm{DoF} \leq 1.5$, combined reconstruction (red) is chosen, otherwise the inner detector standalone reconstruction (blue).

helpful, because it is necessary to understand the reconstruction and the Truth information is always correct. Of course the Truth information will not be available in data taking, hence it must not be used for the selection itself. It can only serve as a kind of starting point from which the selection evolves. For the derivation the single muon samples have been used. Similar to equation 4.7 the relative difference of two measured parameters is defined as

$$(\Delta p_T / p_T)^{\mathrm{a,b}} = \frac{p_T^{\mathrm{a}} - p_T^{\mathrm{b}}}{0.5 \cdot (p_T^{\mathrm{a}} + p_T^{\mathrm{b}})}$$

$$\text{where } (\Delta p_T / p_T)^{\mathrm{a,b}} > 0 \text{ if } p_T^{\mathrm{a}} > p_T^{\mathrm{b}} \tag{5.1}$$

In this notation a and b can stand for either of inner detector standalone, muon spectrometer standalone or combined reconstruction. Equation 5.1 is used for describing non-Monte Carlo comparisons, otherwise equation 4.7 is used. In order to find and optimise selection criteria the different reconstruction methods have been compared with each other. If two algorithms do not agree with each other clearly, at least one has not reconstructed the track correctly. Ith might therefore be useful to find out which reconstruction is correct. As a first step, the combined reconstruction is compared with the inner detector reconstruction (figure 5.5).

If, for example, $(\Delta p_T / p_T)^{comb,inner} > 0.5$, then the p_T of the inner detector reconstruction is only about 60% of the p_T from combined reconstructions. This follows from equation 5.1 with

$$
\begin{aligned}
(\Delta p_T / p_T)^{comb,inner} &= \frac{p_T^{comb} - p_T^{inner}}{0.5 \cdot (p_T^{comb} + p_T^{inner})} > 0.5 \\
\Rightarrow \quad p_T^{inner} &< \frac{3}{5} \cdot p_T^{comb}
\end{aligned}
\tag{5.2}
$$

This is a significant deviation, hence it is of importance to find the reason for this behaviour and also the corresponding reconstruction of the muon spectrometer. For the implementation of the selection algorithm one has to know which reconstruction yields the best result for the present event.

From figure 5.6 one sees, that for $(\Delta p_T / p_T)^{comb,inner} > 0.5$ usually the combined reconstruction is better than the inner detector reconstruction; it has clearly less distinct tails and the distribution is much narrower. From plot 5.7 follows, that the χ^2 / DoF distribution is broader than usual, about 50% of the particles have a $\chi^2 / \mathrm{DoF} > 1.5$, which, in principle, indicates a wrong track reconstruction.
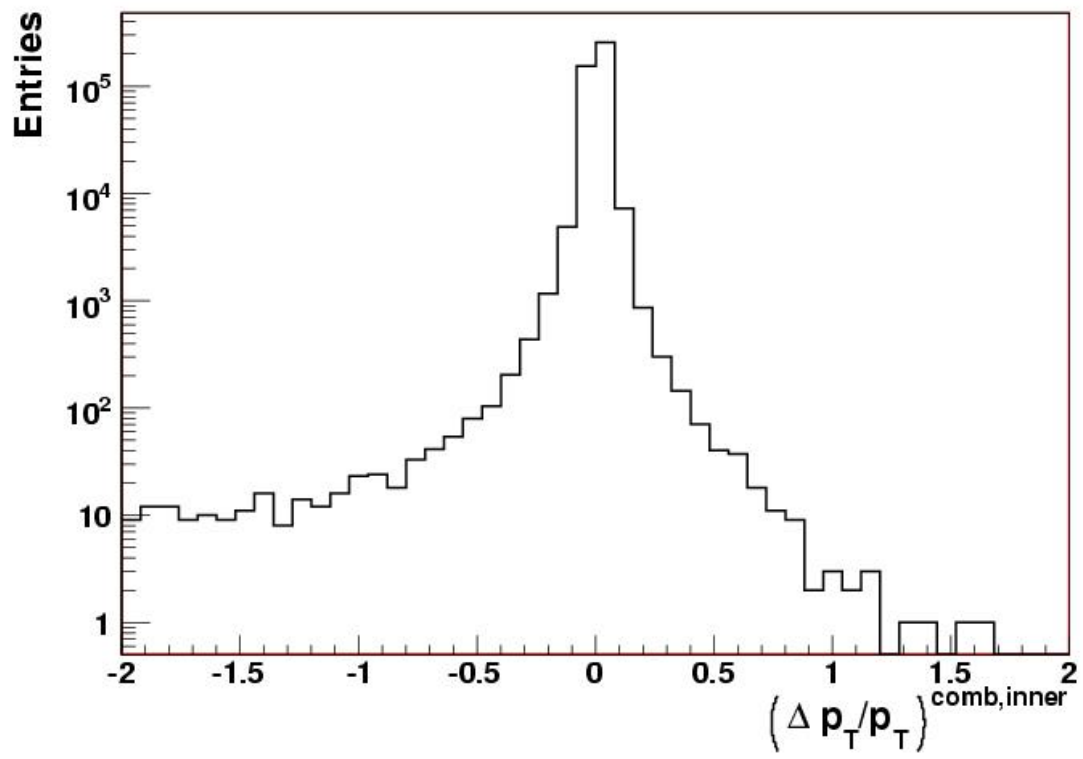
Figure 5.5: Comparison of combined and inner detector reconstruction: $(\Delta p_T / p_T)^{comb,inner}$
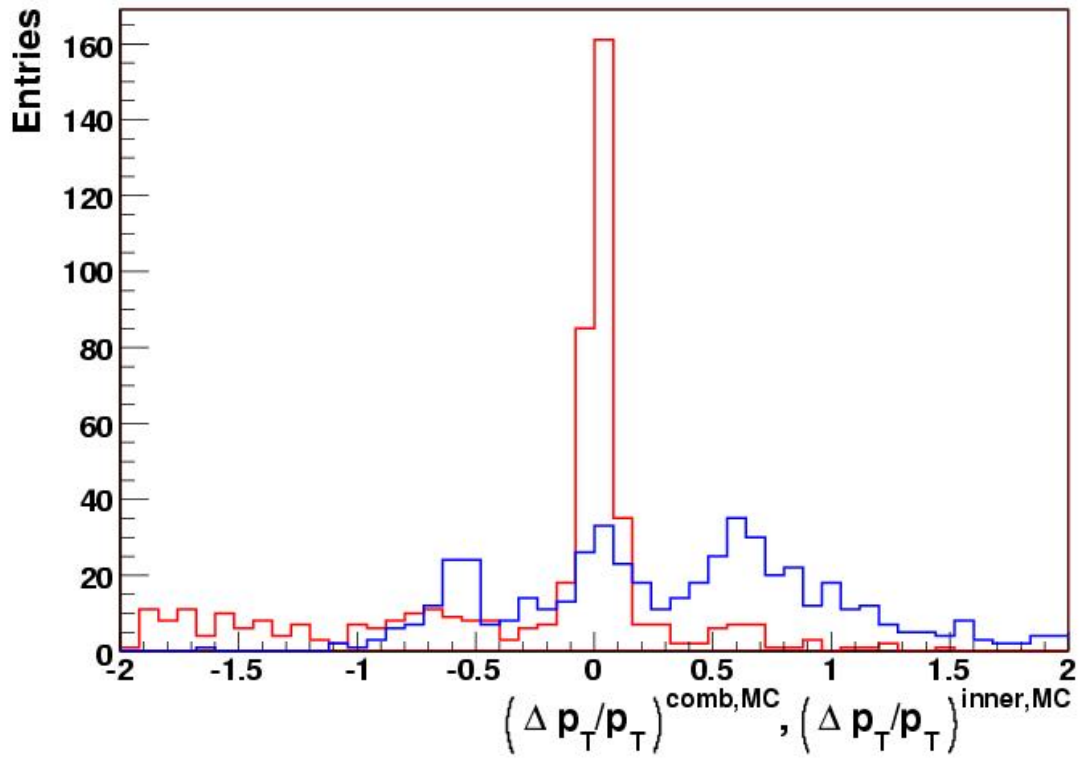
Figure 5.6: Comparison of $(\Delta p_T/p_T)^{comb,MC}$ (red) and $(\Delta p_T/p_T)^{inner,MC}$ (blue) for $(\Delta p_T/p_T)^{comb,inner} > 0.5$
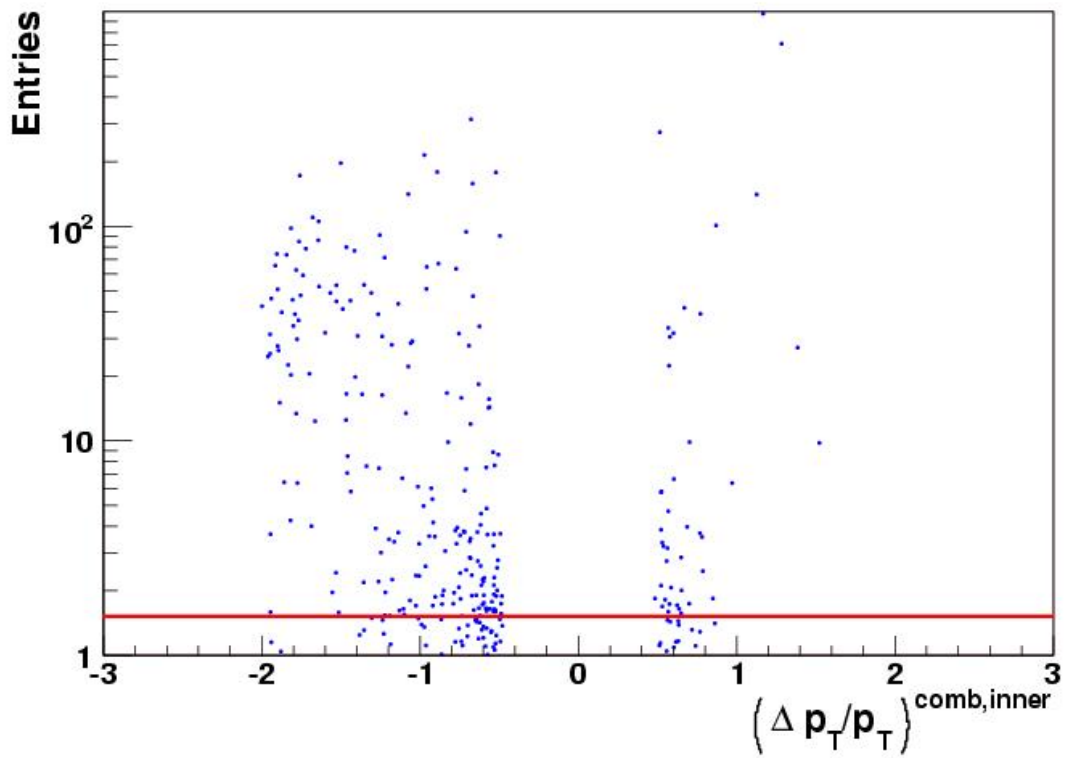
.

Figure 5.7: This plot shows the χ^2/DoF distribution for $(\Delta p_T/p_T)^{comb,inner} > 0.5$. More than 50% of the particles have a $\chi^2/$DoF larger than 1.5.
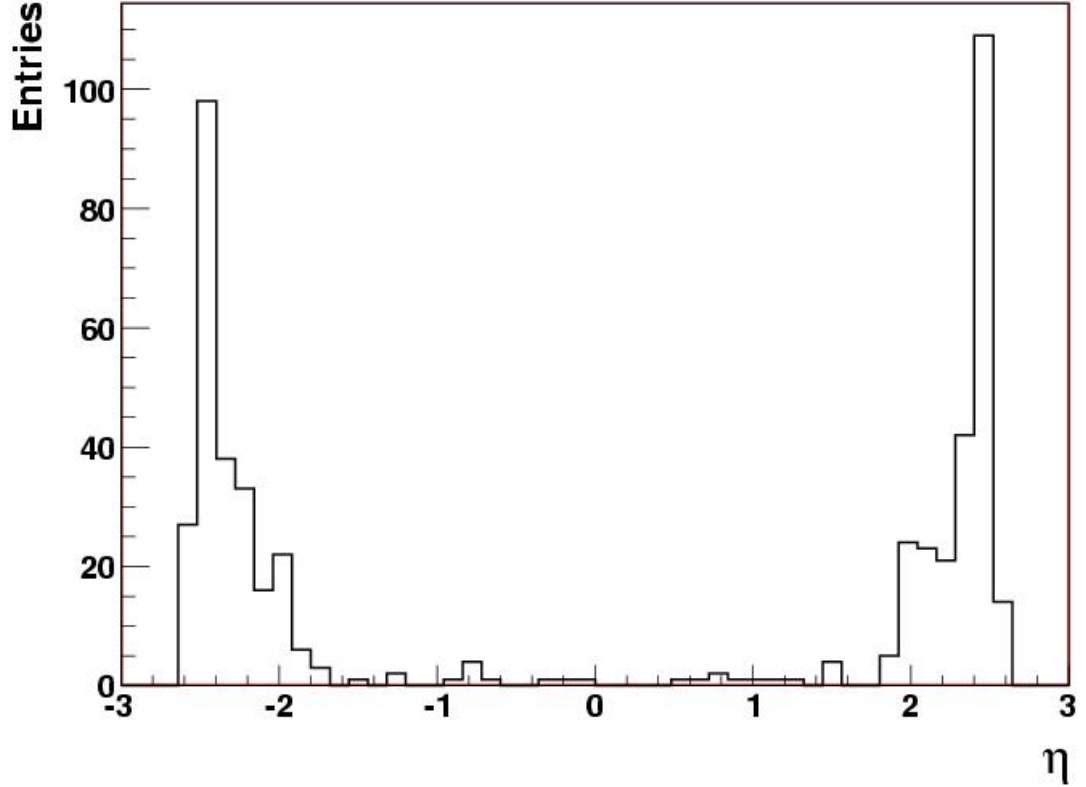
Figure 5.8: This plot shows the η distribution for $(\Delta p_T/p_T)^{comb,inner} > 0.5$

For those particles where $(\Delta p_T/p_T)^{comb,inner} > 0.5$ the η distribution is shown in figure 5.8. It is obvious, that nearly all particles have $|\eta| > 2$ which means that those tracks point in forward direction. In that area the inner detector is nearly insensitive, which explains that result. The fact that the combined reconstruction yields a good result despite the inner detector reconstruction being not so good means that the combination mainly uses the muon spectrometer reconstruction. These results motivate the comparison between muon spectrometer and inner detector reconstruction. Hence the following definition is useful:

$$\alpha = \frac{p_T^{comb} - p_T^{muon}}{p_T^{inner} - p_T^{muon}} \tag{5.3}$$

The values of α are continuous but peak at $\alpha = 0$ if $p_T^{comb} = p_T^{muon}$ and at $\alpha = 1$ if $p_T^{comb} = p_T^{inner}$. Therefore the distribution of α (figure 5.9) allows conclusions about the particular weightings for the combination of inner detector reconstruction and muon spectrometer reconstruction. In MuID the track parameters are not determined by a weighted average of the muon spectrometer and the inner detector track but by a combined refit of the hits in both subdetectors. Therefore α is not limited to $0 \leq \alpha \leq 1$ and only qualitatively indicates the weight of the two detectors. This can be used as a criterion for the quality of the certain reconstruction and hence serve as a further selection criterion. If $|\alpha| < 0.2$ the use of the combined reconstruction is preferred over the inner detector standalone reconstruction, because in that case the muon spectrometer standalone reconstruction resembles the combined reconstruction. On the other hand, if $\alpha \approx 1$, not necessarily the inner detector standalone reconstruction has to be preferred over the combined reconstruction, even if inner detector standalone and combined reconstruction values resemble, this behaviour is shown in figure 5.10.

This means, that for $|\alpha| \geq 0.2$ in general the decision of which reconstruction method to choose is not so clear. Hence another selection criterion is needed. As mentioned earlier, the inner detector is not sensitive in the area $|\eta| > 2$. Therefore the use of the inner detector is not reasonable, but the use of the combined reconstruction. Otherwise in the region where $|\eta| \leq 2$, the use of inner detector standalone reconstruction is to be preferred over combined reconstruction. Combining the selection criteria which have been developed in this chapter yields:

$$
\begin{aligned}
\chi^2/\text{DoF} \quad &\geq 1.5 & &\Rightarrow p_T^{inner} \\
\chi^2/\text{DoF} \quad &< 1.5 \quad \wedge \quad |\eta| \geq 2 & &\Rightarrow p_T^{comb} \\
\chi^2/\text{DoF} \quad &< 1.5 \quad \wedge \quad |\eta| < 2 \quad \wedge \quad |\alpha| \geq 0.2 \quad &&\Rightarrow p_T^{inner} \\
\chi^2/\text{DoF} \quad &< 1.5 \quad \wedge \quad |\eta| < 2 \quad \wedge \quad |\alpha| < 0.2 \quad &&\Rightarrow p_T^{comb}
\end{aligned}
\tag{5.4}
$$

By this selection the number of reconstructed particles in the tail of the p_T spectrum is reduced drastically. The accuracy of the reconstruction is improved and the risk of misidentifying an event drops. Figure 5.11 shows the result of the selection, so using the selection reduces the background and so the probability of identifying real leptoquark events rises.

The α-selection has been developed using single muon samples. They do not contain any other particles and hence are useful for calibration and finding optimal parameters for the algorithm. Experimentally single muon events will not occur in the ATLAS experiment, therefore the benefit of the selection is demonstrated on physics samples. Figure 5.12 shows the application of the α-selection and for comparison $(\Delta p_T/p_T)^{comb,MC}$ of a $Z/\gamma^* \to \mu\mu$ sample. Again, it has to be stressed, that
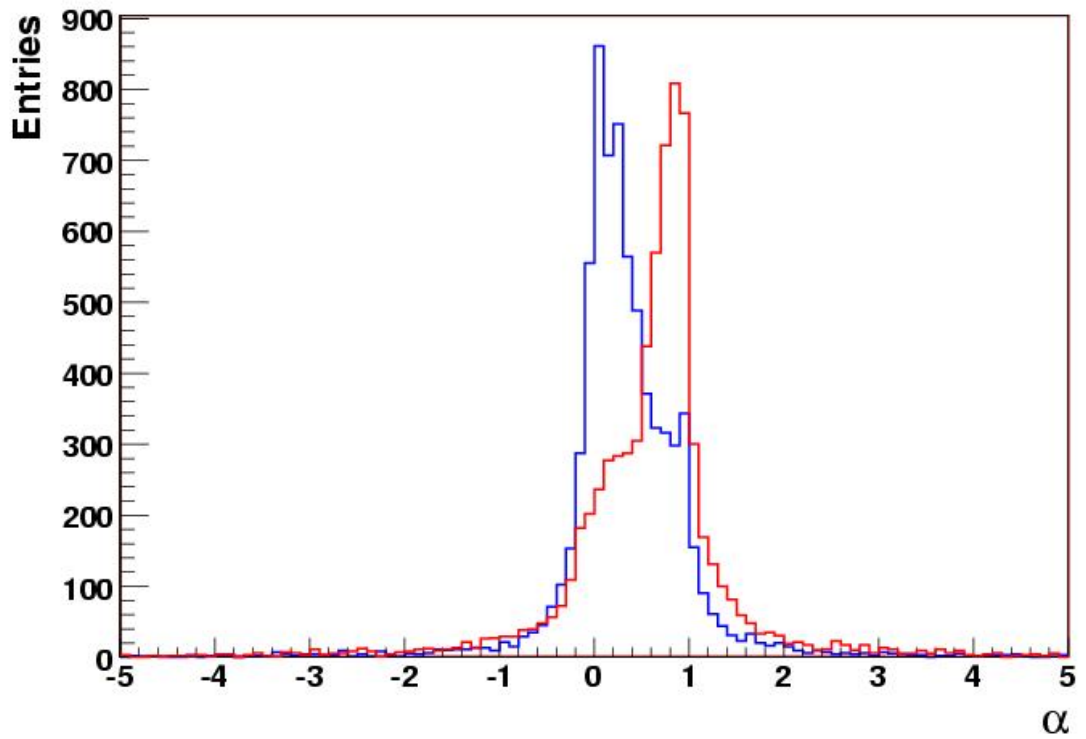
Figure 5.9: This plot shows the α-distribution for $p_T^{MC} = 100$ GeV (red) and $p_T^{MC} = 300$ GeV (blue). Here $\alpha = 0$ means, that $p_T^{comb} = p_T^{muon}$ and $\alpha = 1$ means $p_T^{comb} = p_T^{inner}$.
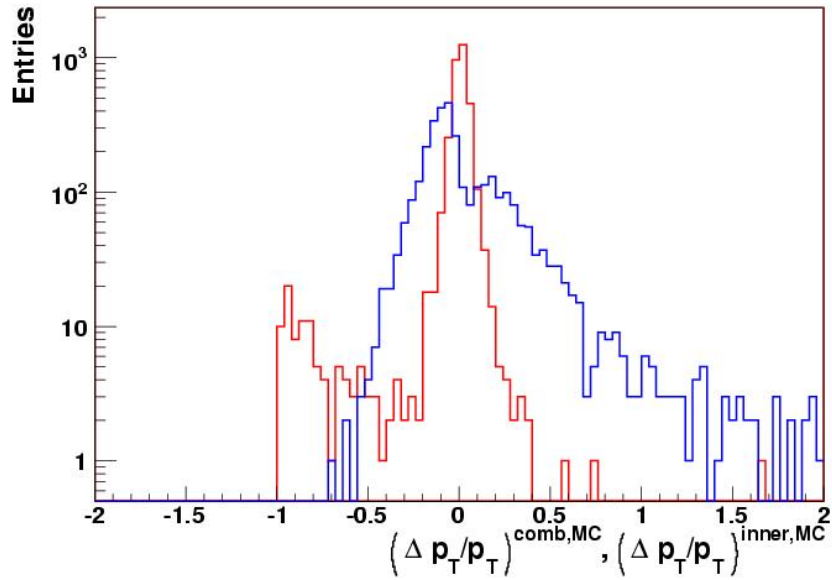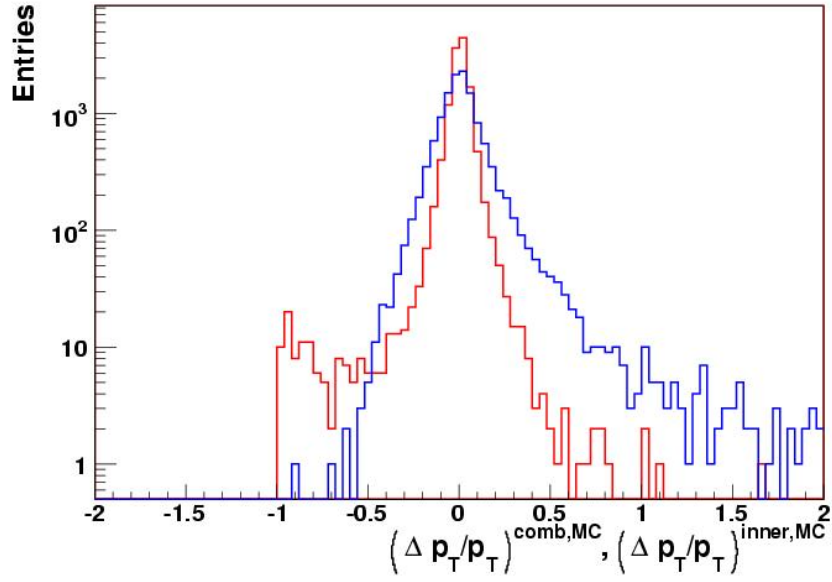
Figure 5.10: Comparison of $(\Delta p_T/p_T)^{comb,MC}$ (red) and $(\Delta p_T/p_T)^{inner,MC}$ (blue) for $|\alpha| < 1.2$ (upper plot) as well as for $|\alpha| < 0.2$ (lower plot).
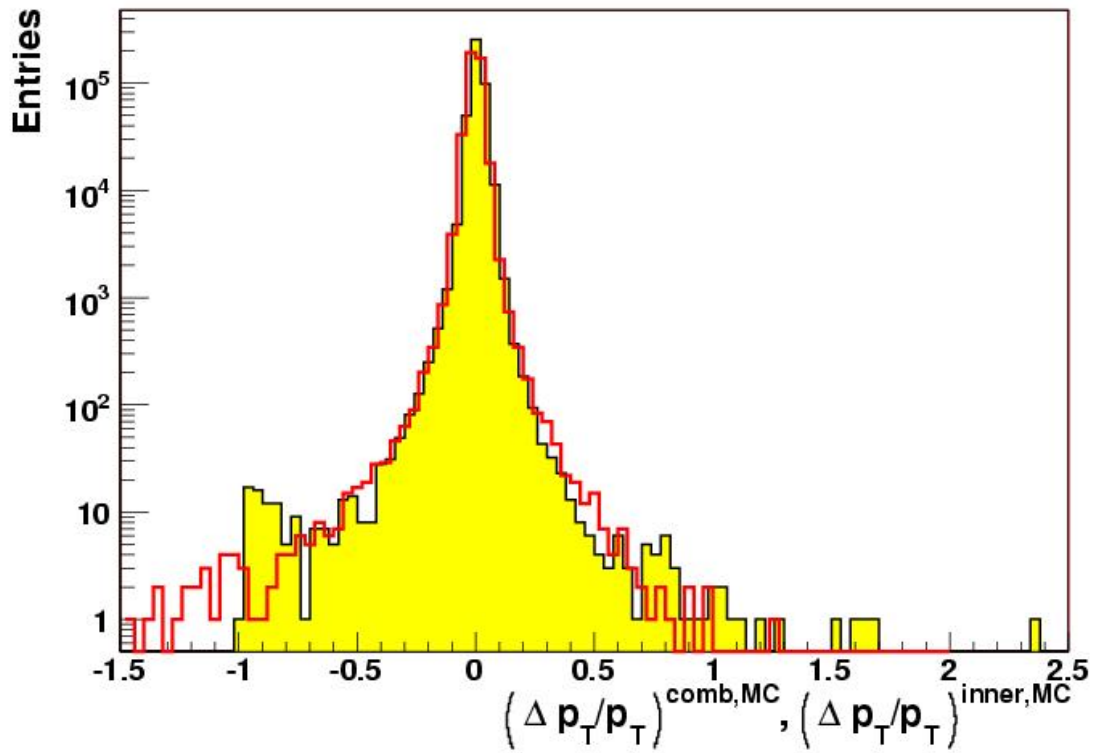
Figure 5.11: This plot shows the relative p_T distribution after the selection from equation 5.4 and for comparison $(\Delta p_T/p_T)^{comb,MC}$ for the Single muon samples.
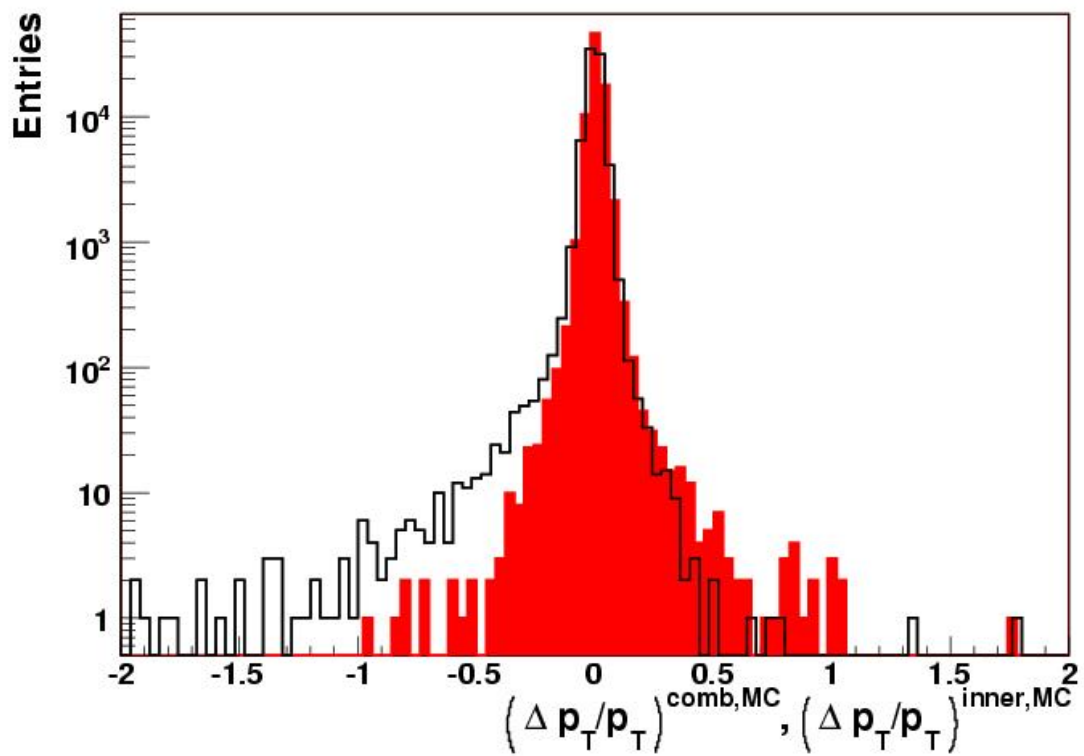
Figure 5.12: This plot shows the application of the α-selection on a physics sample, namely a $Z/\gamma^* \to \mu\mu$ sample. The red curve shows $(\Delta p_T/p_T)^{comb,MC}$, while the black curve shows the $(\Delta p_T/p_T)$ distribution for combined and inner detector reconstruction, depending on the α selection.
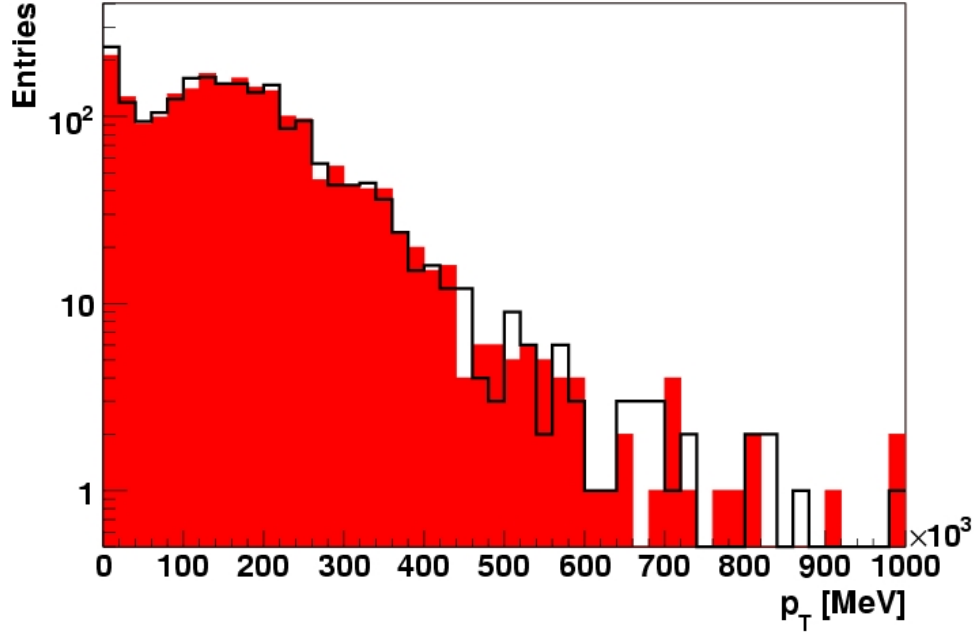
Figure 5.13: This plot shows the reconstructed p_Ts from combined reconstruction (black) and the reconstructed p_Ts after the α-selection which means either p_T^{inner} or p_T^{comb}.

no event has been thrown away, both curves contain exactly the same number of events. The number of muons with overestimated p_T has been reduced drastically, which is the main purpose of the algorithm. It has not been optimised to also reduce underestimated p_Ts as they can not fake a signal for a very high-energetic event like leptoquark production, respectively leptoquark decay. The effect of the α-selection on the leptoquark samples is quite small, but this is the expected behaviour. The muons from leptoquark decays have a high p_T and therefore their number shall not be reduced by any selection. Especially the selection must not replace correctly reconstructed high-p_T muons with underestimated low-p_T muons. Hence, applying the α-selection onto a leptoquark sample, the number of particles in the tail is relatively constant, see figure 5.13.

p_T^{MC} intervals [GeV]	<15	15-22	22-30	30-38	38-45
	45-55	55-65	65-75	75-85	85-95
	95-105	105-125	125-145	145-165	165-185
	185-205	205-225	225-245	245-265	265-285
	285-305	305-325	>325		

Table 5.1: This table shows the fragmentation of the Monte Carlo spectrum used for the interval-method. The intervals including a Monte Carlo sample are highlighted in blue.

5.3 Introduction and Application of the Weighting Method

The weighting method is an algorithm which allows the calculation of probabilities for the momentum reconstruction. It is based on determining probabilities that a particle with a given Monte Carlo Truth p_T results in a mean momentum $p_T^{measured}$. The advantage of this method is that it only depends on the statistics of the sample used to calculate the probabilities – but not on the statistics of the sample on which the weighting is applied. It has been mentioned earlier, that only few events are reconstructed in the tails of the p_T-distribution, because of the large $Z \to \mu\mu$ cross section these events are still an important background. In order to gain significant results high statistics is necessary, but currently the statistics available is not sufficient. Thus the weighting method will be applied on the muon reconstruction in order to check the effects of the results from the last chapter on physics events $(Z/\gamma^* \to \mu\mu)$. results from the last chapter. The probabilities are calculated from the single muon samples. These samples have p_Ts of 10, 18, 26, 50, 100 and 300 GeV. Each of these samples is produced with fixed transverse momentum, results for the other p_T values are derived by linear interpolation. The results will then be applied to physics samples. The low statistics requires to calculate probabilities for the particles reconstructed p_T as a function of p_T^{MC} intervals (so called "weighting") for the inner detector as well as for the combined reconstruction.

At first the Monte Carlo spectrum has to be divided into intervals. These intervals are nearly equidistant, see table 5.1 for details. Then the spectrum of the measured p_Ts has been subdivided into 24 intervals. This is done using a linear approach with the interval boundaries

$$\frac{i}{10} \cdot p_T^{MC} \qquad \text{for} \qquad i = 1 \dots 23 \qquad (5.5)$$

The parameter i denotes the intervals according to table 5.1. The result is the two-dimensional plane of p_T^{MC} and $p_T^{measured}$ as shown in figure 5.14, which conists of 552
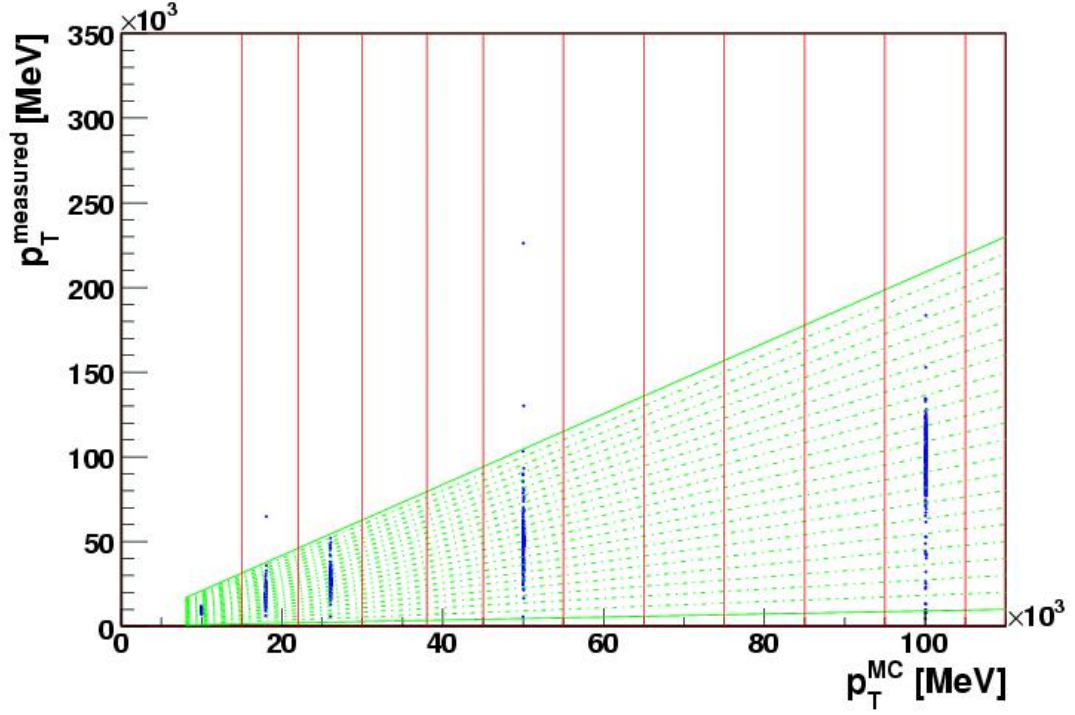
Figure 5.14: This plot shows the Monte Carlo p_T versus the measured p_T. The vertical red lines denote the boundaries for the Monte Carlo intervals and the green lines mark the boundaries for the intervals of $p_T^{measured}$. The number of particles within each box (limited by two green and two red lines) are counted.

trapezoids. Now $p_T^{measured}$ is plotted against p_T^{MC} and the number of entries in each trapezoid is counted. By dividing the number of particles per trapezoid through the total number of particles within each Monte Carlo interval i, the fraction of particles p_{ij} per trapezoid within this interval is calculated. Of course that probabilities have to be normalised. The normalising factor w_j is the sum of the p_{ij} within a interval i. Each column i is then normalised by

$$\tilde{p}_{ij} = \frac{p_{ij}}{w_j} \qquad \text{where} \qquad \sum_i \tilde{p}_{ij} = 1 \qquad (5.6)$$

and $\tilde{p}_{ij}$ is the normalised probability of a particle with a certain Monte Carlo Truth p_T being reconstructed with a certain measured momentum, $p_T^{measured}$.

Figure 5.15 shows the 2-dimensional momentum distribution of the Truth muons (p_T^{MC}) and their reconstructed momentum, $p_T^{measured}$. This means, that for each Monte Carlo muon in each bin of the 24 bins of the corresponding row i of p_T^{MC} the number of entries has been increased by $\tilde{p}_{ij} \cdot 1$. Thus each p_T^{MC} leads to 24 entries of $p_T^{measured}$. The result represents the distribution of $p_T^{measured}$ which has been calculated from the Monte Carlo Truth information. In the lower plot of figure 5.15 the application of the weighting method applied onto a $Z \to \mu\mu$ sample is shown. The upper plot contains the relative difference of combined reconstruction and Monte Carlo Truth, $(\Delta p_T / p_T)^{comb,MC}$, after weighting. The lower plot shows the distribution of the reconstructed p_Ts after weighting and applying the α-selection. By comparing both plots one sees, that the number of entries in the central area rises after applying the selection (for example, compare p_T^{MC} interval 12 of both plots).

5.4   Results

In this chapter the α-selection for choosing the optimal reconstruction method for each muon has been developed. The algorithm uses a combination of χ^2-, η- and p_T-selection. It has been applied to single muon samples and physics samples – namely a $Z/\gamma^* \to \mu\mu$ and a leptoquark sample. The result is a reduction of the misreconstructed muons with overestimated p_T for both, STACO and MuID reconstruction, as shown for a Z/γ^* sample in figure 5.16. It has to be stressed that no events are thrown away, meaning that no cuts are applied but the better reconstruction algorithm – inner detector standalone or combined reconstruction – is selected instead. Thereafter a weighting method has been introduced whose aim is the application of the selection onto the samples which have too low statistics. This is done by calculating the probability of reconstructing a certain p_T for a given Monte Carlo Truth momentum. The application of this method shows the same results as the plain reconstruction and weighting – just as expected. But the weighted selection now uses only the Monte Carlo information and is virtually independent from the available statistics. Only the calculation of the probabilities from the Monte Carlo Truth information depends on the statistics.
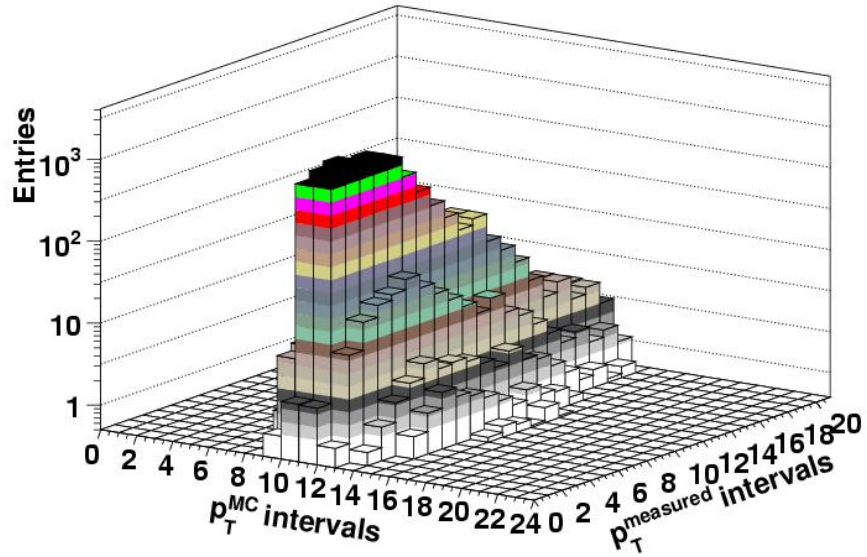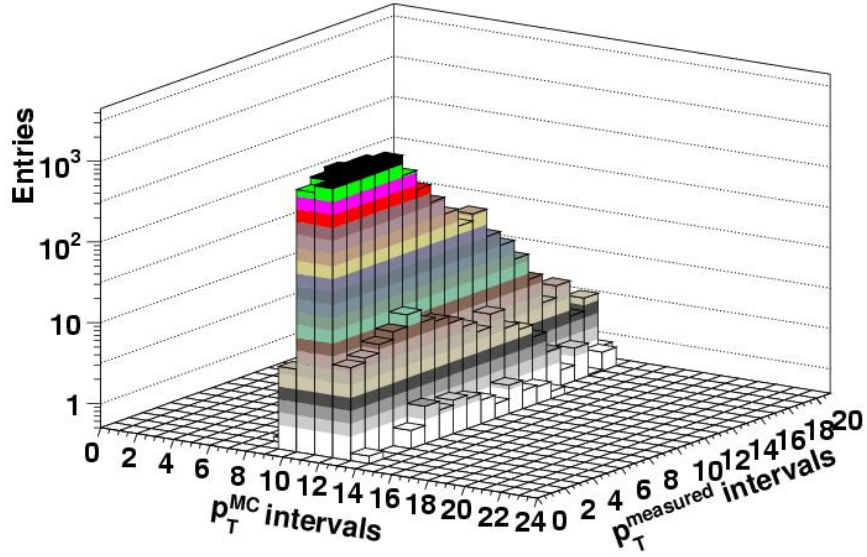
Figure 5.15: The upper plot shows $(\Delta p_T / p_T)^{comb,MC}$ after weighting. The lower plot shows the result of the α-selection after weighting. The $Z \rightarrow \mu\mu$ sample has been used.
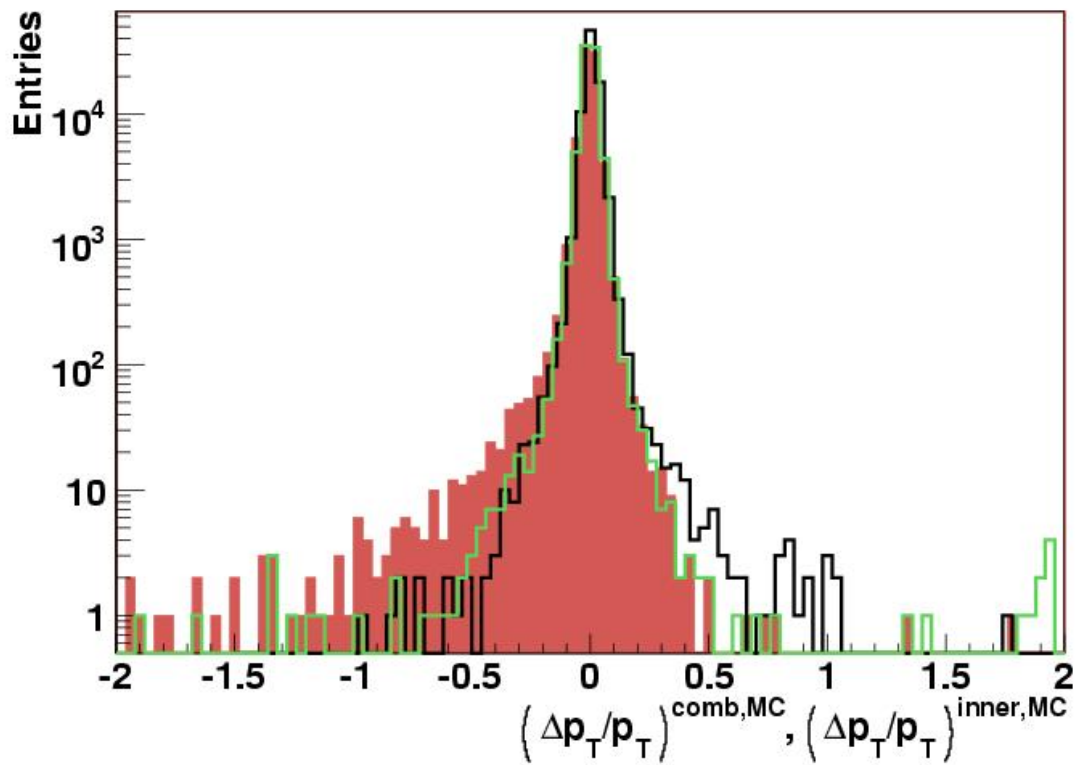
Figure 5.16: This plot shows a comparison of the α-selection for STACO (green) and MuID (red) reconstruction for the $Z/\gamma^* \to \mu\mu$ sample. The selection works slightly better with MuID reconstruction but in both cases the number of muons in the tail is reduced. The black curve shows the distribution of $(\Delta p_T/pT)^{comb,MC}$ for comparison. For STACO the selection also reduces the tail of the underestimated p_Ts.

6 Summary and Outlook

The topic of this thesis is the study of the muon reconstruction and their influence on a possible signal of leptoquarks. The study has been performed within the upcoming ATLAS experiment at the Large Hadron Collider at CERN. This analysis used exclusively Monte Carlo-simulated events. The majority of these events were produced within the Computing Service Challenge, a worldwide distributed effort of the involved institutes on testing and optimising the computing infrastructure of the experiment. The precise muon reconstruction will be a crucial task for ATLAS, mainly because many interesting decay modes include muons. For example the Higgs-Particle, has a decay mode $H \to ZZ \to \mu\mu\mu\mu$. Leptoquarks can also decay into muons (and jets), hence the muons must be reconstructed precisely in order to identify the original particle correctly.

In the first part of this thesis two reconstruction algorithms have been compared, namely STACO and MuID. The focus was on overestimated momenta which easily could contribute to a fake leptoquark signal. This comparison was performed using single muon samples as well as physics samples, namely a $Z/\gamma^* \to \mu\mu$ and a leptoquark sample. Both algorithms yield nearly identical results for combined reconstruction and STACO seems to have a slightly better performing muon standalone reconstruction. In the second part, an algorithm – the so-called α-selection – to choose the optimal reconstruction for different classes of muons has been developed. Among the muons which could be classified as potentially mismeasured (e.g. large χ^2) most are reconstructed correctly and throwing them away would reduce the statistics. Thus a simple cut would reduce the probability of discovering new physics. The α-selection is based upon a combination of the estimation of the muon's track quality (expressed through the χ^2), the η-direction of the track and a parameter α which describes the difference between muon spectrometer standalone, inner detector standalone and combined reconstruction. This selection reduces the number of muons with overestimated p_T significantly and hence optimises the quality of reconstruction. The influence of the selection on muons from leptoquark decay has been studied. It has been shown that it does not lead to an additional classification of real high p_T muons as having a lower p_T. Thus the risk of misreconstructed muons leading to a fake leptoquark signal is reduced. The statistics of the

generated Monte Carlo sample is not sufficient to study the improvements of the algorithm on $Z/\gamma^* \to \mu\mu$ events, therefore a weighting method has been applied. Here the probability of reconstructing a certain $p_T^{measured}$ depending on the Monte Carlo Truth p_T has been calculated. This method allows us to investigate the muon reconstruction in a manner which is virtually independent of the available statistics. In this vein the results obtained from the selection could be verified. From studies presented here the following conclusions can be drawn: The default reconstruction algorithms implemented in the ATLAS software work very well, but focus on the complete p_T-spectrum, hence for high p_Ts there is a possibility of misreconstruction. The presented selection can improve the results of the reconstruction especially for high-energetic muons, like they can appear at the search for new physics.

As an outlook, the results can be used for muon identification in a continuative leptoquark analysis which also includes the reconstruction of jets.

A   The χ^2-Method

This appendix introduces the χ^2-method as it has been used frequently throughout this thesis. This overview follows [26]. In statistics and error analysis probability distributions like the normal distribution, the binomial distribution or the Poisson distribution are commonly used. These distributions describe the expected results of an experiment when repeated very often, which basically means they base on the central limit theorem. A well known example is the statistics of dice throws, where the numbers rolled resemble a binomial distribution. The aim of the χ^2-method is to test, if the measured values coincide with the expected values.

If the x_k are k independent, normal distributed measured values which have a mean $\bar{x}_k$ and a variance σ_k^2, the $\tilde{\chi}^2$ is defined as:

$$\tilde{\chi}^2 = \sum_{k=1}^{n} \frac{(x_k - \bar{x}_k)^2}{\sigma_k^2} \tag{A.1}$$

In this definition it is summed over all parameters n. The number of parameters is reduced by constraints c which yields the degrees of freedom (DoF). In a system which is described by an unambiguously set of parameters, each parameter is called a degree of freedom. It can be shown, that the expected mean value of $\tilde{\chi}^2$ exactly equals the number of degrees of freedom

$$\langle \tilde{\chi}^2 \rangle = DoF \tag{A.2}$$

This does not mean, that one can expect to get $\tilde{\chi}^2 = DoF$, but that for a infinitely repeated measurement, for which always the $\tilde{\chi}^2$ has been calculated, the mean value of these $\tilde{\chi}^2$ would equal DoF. Nonetheless, even after only one series of measurement the comparison of $\tilde{\chi}^2$ and DoF is a good indicator for the correlation. It is quite improbable, that $\tilde{\chi}^2$ is much larger than DoF if the expected distribution is the correct one. So, if $\tilde{\chi}^2 \gg DoF$, the expected distribution is quite probably the false one. This insight motivates another definition, the so called *reduced* χ^2:

$$\chi^2 = \frac{\tilde{\chi}^2}{DoF} \tag{A.3}$$

Because $\langle \tilde{\chi}^2 \rangle = DoF$, one gets

$$\langle \chi^2 \rangle = 1 \tag{A.4}$$

In this way the test can be interpreted independently from the degrees of freedom: if $\chi^2 \approx 1$ (or less), one can assume the expected distribution to be correct. On the other hand, if $\chi^2 \gg 1$ most probably the expected distribution might be false or the errors wrong.

When using STACO, the degrees of freedom always equal five, as the χ^2 is the solution of equation 4.6, which has five parameters.

B Samples used for this study

This study has been realised using samples created within the Rome production in Athena 10.0.x as well as with samples from the Commissioning Service Challenge (CSC). The CSC samples used have been produced with Athena 11.0.42, which were the best available at the time of this study.

The Single Muon samples (which have fixed p_T values) consist of:

- mc11.004042.mu_pt10

- csc11.007216.singlepart_mu18

- csc11.007222.singlepart_mu26

- csc11.007231.singlepart_mu50

- mc11.004934.mu_pt100

- mc11.004946.mu_pt300

The Physics Samples used were standard $Z/\gamma^* \to \mu\mu$ samples:

- csc11.005145.PythiaZmumu

- rome.004122.recov10NONT.Sherpa_ZJ1mumu

The leptoquark samples used throughout this study have been produced privately at the Ludwig-Maximilians-Universität München.

List of Figures

List of Tables

Bibliography

[1] CHRISTIANSEN, T.: *Search for Second-Generation Leptoquarks in p$\bar{p}$ Collisions*, Ludwig-Maximilians-Universität München, Diss., 2003 2.1, 1

[2] KUZE, M. ; SIROIS, Y.: *Search for Particles and Forces Beyond the Standard Model at HERA ep and Tevatron p$\bar{p}$ Colliders.* 2002. – DESY Preprint 2.1

[3] MITSOU, V. A. ; BENEKOS, N. Ch. ET AL: *Prospects for scalar leptoquark discovery at the LHC.* In: *Czech. J. Phys.* 55 (2005) 2.2, 2.4

[4] GEORGI, H. ; GLASHOW, S. L.: *Unity of All Elementary-Particle Forces.* In: *Phys. Rev. Lett.* 32 (1974), Nr. 8, p. 438 2.2

[5] PATI, J. C. ; SALAM, A.: *Lepton number as the fourth color.* In: *Phys. Rev. D* 10 (1974), Nr. 1, p. 275 2.2

[6] BUCHMÜLLER, W. ; WYLER, D.: *Constraints on SU(5)-type leptoquarks.* In: *Phys. Lett. B* 177 (1986), p. 377 2.2

[7] DIMOPOULOS, S. ; SUSSKIND, L.: *Mass without scalars.* In: *Nucl. Phys. B* 155 (1979) 2.2

[8] DIMOPOULOS, S.: *Technicolored Signatures.* In: *Nucl. Phys.* B 168 (1980) 2.2

[9] EICHTEN, E. ; LANE, K.: *Dynamical breaking of weak interaction symmetries.* In: *Phys. Lett. B* 90 (1980) 2.2

[10] ANGELOPOULOS, V. D. ; ELLIS, J. ET AL: *Search for new quarks suggested by the superstring.* In: *Nucl. Phys. B* 292 (1987) 2.2

[11] HEWETT, J. L. ; RIZZO, T. G.: Low-energy phenomenology of superstring-inspired E_6 models. In: *Physics Reports* 183 (1989) 2.2

[12] BUCHMÜLLER, W. ; RÜCKL, R. ET AL: *Leptoquarks in Lepton-Quark Collisions.* In: *Phys. Lett. B* 191 (1987). – Erratum-ibid. B 448 (1999) 2.3

[13] BLÜMLEIN, J. ; BOOS, E. ET AL: *Leptoquark Pair Production in Hadronic Interactions.* In: *Z Phys C* 76 (1997) 2.4

[14] ACOSTA, D. E. ; BLESSING, S. K.: *Leptoquark Searches at HERA and the Tevatron.* In: *Annu. Rev. Nucl. Part. Sci* 49 (1999) 2.5

[15] FRAUENFELDER, H. ; HENLEY, E.M.: *Teilchen und Kerne.* 4th edition. Oldenbourg, 1999

[16] PERKINS, D.: *Introduction to High Energy Physics.* 3rd edition. Addison Wesley, 1987

[17] KNOBLOCH, J.: *LHC Computing Grid. Technical Design Report* / CERN. 2005. – Technical Report 3.2

[18] SJÖSTRAND, T. ; EDEN, P. ET AL: Pythia 6.2 Physics and Manual. In: *Computer Physics Commun.* 135 (2001) 3.3

[19] EIDELMAN, S. ET AL: *Review of Particle Physics.* In: *Physics Letters B* 592 (2004). http://pdg.lbl.gov 4, 11

[20] CERN: *public web page.* http://www.cern.ch 4.1, 4.2, 4.5, 4.6

[21] SCHOTT, M. ; DUCKECK, G. ET AL: *Study of the Sagitta Resolution of MDT-Chambers with Cosmic Muons.* – ATLAS Note 4.2.3

[22] ADAMS, D. ; ASSAMAGAN, K. ET AL: *Track Reconstruction in the ATLAS Muon Spectrometer with MOORE* / ATLAS. 2003. – Technical Report 9

[23] FORMICA, A.: *Design, implementation and deployment of the Saclay muon reconstruction algorithms (Muonbox/y) in the Athena software framework of the ATLAS experiment.* – cs.CE/0306105 9

[24] LAGOURI, Th. ; ADAMS, D. ET AL: *Reconstruction Procedure for the ATLAS Detector at the LHC at CERN* / ATLAS. 2003. – Technical Report 10

[25] THE ATLAS COLLABORATION: *ATLAS Detector and Physics Performance Technical Design Report* / CERN. 1999. – Technical Report 10

[26] TAYLOR, John R.: *Fehleranalyse: Eine Einführung in die Untersuchung von Unsicherheiten in physikalischen Messungen.* 1st edition. VCH, 1988 A

Acknowledgements

Zum Schluß möchte ich mich bei den Personen bedanken, die maßgeblich zum Gelingen dieser Diplomarbeit beigetragen haben. Ein herzliches Dankeschön geht an...

- Prof. Dr. Dorothee Schaile für die Möglichkeit, die Diplomarbeit an ihrem Lehrstuhl zu verfassen, sowie für die Erstellung des Erstgutachtens.

- Prof. Dr. Dieter Lüst für die Erstellung des Zweitgutachtens.

- Dr. Raimund Ströhmer für die ausgezeichnete Betreuung sowie viele Tips und Ratschläge während des letzten Jahres.

- Gernot Krobath und Dr. Felix Rauscher für die gute Büroatmosphäre, viele Diskussionen und Ratschläge.

- Dr. Raimund Ströhmer, Gernot Krobath und Dr. John Kennedy für das Korrekturlesen dieser Arbeit.

- Dr. Johannes Elmsheuser, Dr. John Kennedy und Dr. Günther Duckeck für die wertvolle Hilfe bei Computerproblemen aller Art.

- Herta Franz, unsere Sekretärin, die immer mit Rat und Tat zur Seite stand.

- den Lehrstuhl für Elementarteilchenphysik sowie alle Leute, die ich dort bisher kennenlernen durfte: Otmar Biebel, Meta Binder, Philippe Calfayan, Tim Christiansen, Jörg Dubbert, Günter Duckeck, Johannes Elmsheuser, Frank Fiedler, Daniela Görisch, Alexander Grohsjean, Petra Haefner, Ralf Hertenberger, John Kennedy, Gernot Krobath, Marion Lambacher, Martin Lamprecht, Raphael Mameghani, Doris Merkl, Alexander Mlynek, Thomas Müller, Thomas Nunnemann, Matthias Obermaier, Felix Rauscher, Gaby Reiter, Dorothee Schaile, Philipp Schieferdecker, Matthias Schott, Cedric Serfon, Raimund Ströhmer, Britta Tiller, Attila Varga und Fritz Vollmer.

- meine Eltern sowie meine Familie für die großartige Unterstützung.

- meine Freundin Susanne dafür, daß sie immer da ist und mich in stressigen Zeiten aufgebaut hat.

- meine Freunde und alle Leute von SnakeNet. \m/

- Lemmy Kilmister, James Hetfield, Peter Tägtgren, John Coltrane, Johann Hegg, Mikael Åkerfeldt und deren Bands für die gute Musik.

Selbständigkeitserklärung

Ich versichere hiermit, die vorliegende Arbeit selbständig verfaßt zu haben und keine anderen als die angegebenen Quellen und Hilfsmittel verwendet zu haben.

Benjamin Ruckert

München, den 27. Juli 2006